STUDY OF COMPACT TUNABLE FILTERS USING NEGATIVE REFRACTIVE INDEX TRANSMISSION LINES

A Thesis

by

BRIAN PATRICK LEWIS

Submitted to the Office of Graduate Studies of
Texas A&M University
in partial fulfillment of the requirements for the degree of

MASTER OF SCIENCE

May 2011

Major Subject: Electrical Engineering

Study of Compact Tunable Filters Using Negative Refractive Index Transmission Lines

STUDY OF COMPACT TUNABLE FILTERS USING NEGATIVE REFRACTIVE INDEX TRANSMISSION LINES

A Thesis

by

BRIAN PATRICK LEWIS

Submitted to the Office of Graduate Studies of
Texas A&M University
in partial fulfillment of the requirements for the degree of

MASTER OF SCIENCE

Approved by:

Chair of Committee,	Kai Chang
Committee Members,	Robert D. Nevels
	Jun Zou
	Roger Smith
Head of Department,	Costas N. Georghiades

May 2011

Major Subject: Electrical Engineering

ABSTRACT

Study of Compact Tunable Filters Using Negative Refractive Index Transmission Lines. (May 2011)

Brian Patrick Lewis, B.S., Texas A&M University

Chair of Advisory Committee: Dr. Kai Chang

Today's microwave circuits, whether for communication, radar, or testing systems, need compact tunable microwave filters. Since different microwave circuit applications have radically different size, power, insertion loss, rejection, vibration, and thermal requirements, new filter technologies with different balances between these requirements are always desirable. Negative Refractive Index (NRI) transmission media was discovered 10 years ago with the unique property of negative phase propagation. A literature review was conducted to identify potential NRI methods for filters and other devices, but no NRI tunable filters were found. To address this gap, a family of tunable NRI bandpass filters was simulated and constructed successfully using end-coupled zeroth order resonators. Tuning was accomplished by controlling the negative phase length of the NRI sections with varactors. The resulting L-band filters exhibited a 25-40% tunable range, no higher order resonances, and required only one fourth the length of a coupled-line filter constructed from traditional 180 degree microstrip resonators.

DEDICATION

This thesis is dedicated to my newborn daughter, Siwella, who provided the final motivation for me to finish this thesis.

ACKNOWLEDGEMENTS

Foremost, I would like to thank Dr. Kai Chang for his instruction, support, guidance, and most of all his patience. Next, I would like to express gratitude towards Mr. Ming-Yi Li for his help in fabricating my circuits and the students in Dr. Chang's group for continual help and advice. I would like to thank Drs. Robert D. Nevels, Jun Zou, and Roger Smith for their support, feedback, and participation in my committee. I greatly appreciate Texas A&M University, ERC Inc., ESCG, and the Electromagnetics Branch of Johnson Space Center for providing an environment where I can continually learn and for allowing my education and vocation to each benefit the other. Whenever I felt discouraged, my coworkers encouraged me to finish my thesis. My family and friends never stopped believing I would finish. Special thanks to my wife, Rebecca, for helping me find time to finish my thesis, and most of all to Christ for his provision and love.

NOMENCLATURE

CTL	Composite (right/left-hand) Transmission Line
LH	Left-Handed
LHTL	Left-Handed Transmission Line
NRI	Negative Refractive Index
PRI	Positive Refractive Index
RHTL	Right-Handed Transmission Line
SRF	Self-Resonant Frequency
TL	Transmission Line

TABLE OF CONTENTS

Page

LIST OF FIGURES

LIST OF TABLES

1. INTRODUCTION: ORIGIN OF NEGATIVE REFRACTIVE INDEX MATERIALS

From the time of Maxwell until 2000, human applications of electromagnetics have been governed by the right hand rule, in which the electric field vector, magnetic field vector and direction of propagation form a right hand triplet. In nature, virtually all materials display intrinsic right-handed behavior, therefore researchers had discarded the possibility of the existence of a left-handed (LH) material. However, in 1967, the physicist Veselago proposed the existence of left-handed materials [1]. In his research, he showed that Maxwell's equations did not prohibit simultaneous negative permittivity and permeability, and that the propagation in such a material would be characterized by a left-handed triplet. Unfortunately, no one, including Veselago, could find any material, even theoretical, that would exhibit negative permeability [2]. Negative permittivity had been previously demonstrated by Rotman, but was thought to only be useful for plasma simulation [3]. Veselago's research and publication were considered preposterous and forgotten.

In 1996, Pendry et al. discovered that a mesh of very thin conductors in a periodic lattice with spacing significantly less than a wavelength could produce an effectively negative permittivity [4]. Three years later he discovered a dual structure that demonstrated effectively negative permeability [5],[6]. Finally, in 2000, a research group at the University of California at San Diego rediscovered Veselago's research,

---

This thesis follows the style of *IEEE Transactions on Microwave Theory and Techniques.*

and with consultation from Pendry successfully combined both Pendry's and Rotman's techniques to propose the first artificial Left-Handed Material (LHM) [7], also known as a Negative Refractive Index (NRI) material.

UC-San Diego's initial work included both 2D periodic lattices and 1D periodic transmission lines. They proved not only an additional conduction band between stopbands, but also demonstrated a negative index of refraction by measuring the angle of refraction after passing through an artificial left-handed material [8]. Many other research groups realized the potential of left-handed materials including perfect lenses, improved transmission media and lines, and many novel devices employing negative phase propagation. In the last ten years, research in this area has exploded.

Using the negative phase propagation of an NRI transmission line, improved resonators and filters can be developed. A transmission line resonator will resonate at any frequency where its phase length is an integer multiple of 180 degrees – including zero degrees. It can therefore be realized with a combination of forward and negative phase propagating transmission lines that sum to zero degrees [9],[10]. Resonator-based filters can be designed the same way, using a series of zero-phase length resonators [10]. In addition, the phase length of the NRI segments should be able to be controlled by varying the series capacitance with varactors, allowing for tunable resonators and filters.

2. THEORY OF NEGATIVE REFRACTIVE INDEX MEDIA

2.1 REFRACTION IN POSITIVE AND NEGATIVE REFRACTIVE INDEX MEDIA

Maxwell's equations for a source-free, homogenous, and linear region are as follows in time-harmonic form:

$$\nabla \times \vec{E} = -j\omega\mu\vec{H} \tag{1}$$

$$\nabla \times \vec{H} = j\omega\varepsilon\vec{E} \tag{2}$$

$$\nabla \cdot \vec{E} = 0 \tag{3}$$

$$\nabla \cdot \vec{H} = 0 \tag{4}$$

The two curl equations (1) and (2) can be combined by substitution and simplified using the first divergence equation (3) into a second-order differential equation that is only a function of the electric field:

$$\nabla^2 \vec{E} + \omega^2 \mu\varepsilon\vec{E} = 0 \tag{5}$$

Next, the differential equation can be further simplified by substituting the definition of propagation coefficient:

$$k = \omega\sqrt{\mu\varepsilon} \tag{6}$$

$$\nabla^2 \vec{E} + k^2 \vec{E} = 0 \tag{7}$$

The differential equation can then be solved with a general wave solution. A general wave solution is a product of multiple independent solutions, all oscillatory. Two possible waves exist: forward and backward. If the positive solution is considered for simplicity:

$$\vec{E} = E_0^+ e^{-j\vec{k}\cdot\vec{r}} + E_0^- e^{+j\vec{k}\cdot\vec{r}} = \vec{E}_0 e^{-j\vec{k}\cdot\vec{r}} \tag{8}$$

Substituting the above E-field solution (8) back into Maxwell's first curl equation (1) and simplifying gives the following orthogonal triplet equation:

$$\vec{k} \times \vec{E} = \omega\mu\vec{H} \tag{9}$$

Using the same derivation technique to solve for the magnetic field yields a second orthogonal triplet equation:

$$\vec{k} \times \vec{H} = -\omega\varepsilon\vec{E} \tag{10}$$

Both equations (9) and (10) define k, H, and E as orthogonal, thereby forming either a right-handed or left-handed triplet, depending on the signs of μ and ε. If both are positive, as is true for free space and most natural materials, then a right-handed triplet is formed. If the permeability and permittivity are negative, then a left-handed triplet is formed.

There are two additional possibilities, namely, when μ and ε have opposite signs. Surprisingly, there are naturally occurring cases of this, including plasma, which exhibits negative permittivity [3], and surface plasmons, which exhibit negative permeability [4],[5]. In these cases, the propagation vector *k* becomes imaginary, as the radical will be negative:

$$k = \omega\sqrt{\mu\varepsilon} = j\omega\sqrt{|\mu\varepsilon|} \tag{11}$$

The electric and magnetic fields will then be decaying, not propagating, as seen when this imaginary propagation vector is substituted into the field equations:

$$\vec{E} = \vec{E}_0 e^{-j(j\omega\sqrt{|\varepsilon\mu|}\hat{k})\cdot\vec{r}} = \vec{E}_0 e^{(\omega\sqrt{|\varepsilon\mu|})\hat{k}\cdot\vec{r}} \tag{12}$$

Another interesting property appears when comparing the propagation coefficient and the standard definition of the Poynting Vector (13):

$$\vec{P} = \vec{E} \times \vec{H} \tag{13}$$

When μ and ε are positive, the Poynting vector and propagation vector *k* have the same direction – both form right-handed triplets with E and H. When μ and ε are both negative, then the Poynting vector continues to form a right handed triplet with E and H, indicating that power continues to flow in the same direction, but the propagation vector *k* and the fields form a left-handed triplet, indicating that power flow and phase velocity are in opposite directions, and phase will accumulate in the opposite manner as it does in right-handed materials.

For two- and three-dimensional NRI media, the most visible consequence of negative permeability and permittivity is negative refraction. Normal materials follow Snell's Law, and exhibit positive refraction. These materials can be called Positive Refractive Index (PRI) materials. For ordinary cases, Snell's Law can be derived as follows [11]:

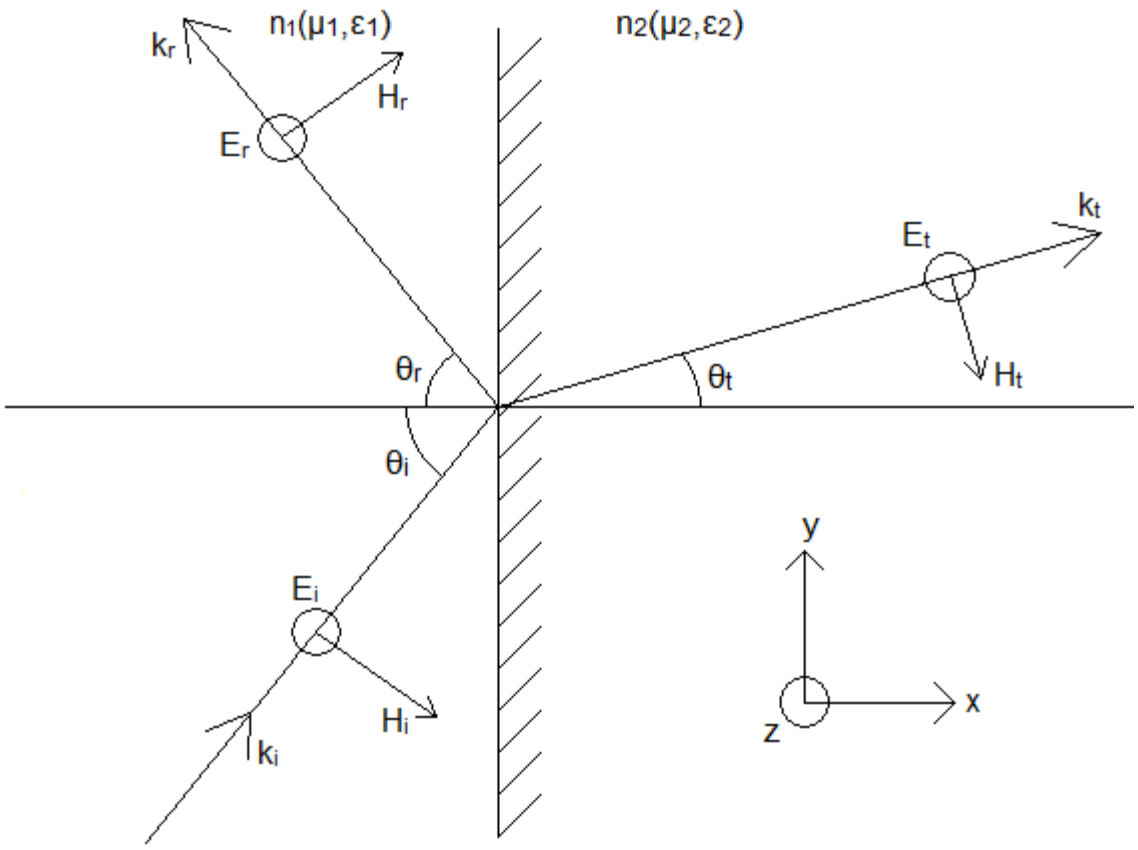

Figure 1: Reflection and refraction at the boundary between two PRI media.

A beam (k_i) in region 1 that is both crossing into region 2 (k_t) and is reflected back into region 1 (k_r) can be broken into electric and magnetic components. In Figure 1, the electric field component is chosen to be tangentially to the boundary for convenience. For this example, using generalized plane waves at the same frequency will allow the frequency term in the exponent to be dropped. Incident, reflected, and transmitted fields are below:

Incident fields:

$$\vec{E}_i = \vec{E}_{0i} e^{-j\vec{k}_i \cdot \vec{r}} \tag{14}$$

$$\vec{H}_i = \vec{H}_{0i} e^{-j\vec{k}_i \cdot \vec{r}} = \frac{1}{\eta_1}(\hat{k}_i \times \vec{E}_{0i} e^{-j\vec{k}_i \cdot \vec{r}}) \tag{15}$$

$$\vec{k}_i \cdot \vec{r} = k_{ix}x + k_{iy}y + k_{iz}z \tag{16}$$

Reflected fields:

$$\vec{E}_r = \vec{E}_{0r} e^{-j\vec{k}_r \cdot \vec{r}} \tag{17}$$

$$\vec{H}_r = \vec{H}_{0r} e^{-j\vec{k}_r \cdot \vec{r}} = \frac{1}{\eta}(\hat{k}_r \times \vec{E}_{0r} e^{-j\vec{k}_r \cdot \vec{r}}) \tag{18}$$

$$\vec{k}_r \cdot \vec{r} = k_{rx}x + k_{ry}y + k_{rz}z \tag{19}$$

Transmitted Fields:

$$\vec{E}_t = \vec{E}_{0t} e^{-j\vec{k}_t \cdot \vec{r}} \tag{20}$$

$$\vec{H}_t = \vec{H}_{0t} e^{-j\vec{k}_t \cdot \vec{r}} = \frac{1}{\eta}(\hat{k}_t \times \vec{E}_{0t} e^{-j\vec{k}_t \cdot \vec{r}}) \tag{21}$$

$$\vec{k}_t \cdot \vec{r} = k_{tx}x + k_{ty}y + k_{tz}z \tag{22}$$

Since the incident, reflected, and transmitted waves are related by their propagation coefficients and are all at the same frequency, equation (23) must hold at all points:

$$k_i = k_r = \frac{\sqrt{\varepsilon_1 \mu_1}}{\sqrt{\varepsilon_2 \mu_2}} k_t \tag{23}$$

At the boundary, the tangential boundary conditions are independent of time and true at all points in the resulting y-z plane. Therefore the exponents of the electric and magnetic field equations must be equal:

$$\vec{k}_i \cdot \vec{r} = \vec{k}_r \cdot \vec{r} = \vec{k}_t \cdot \vec{r} \tag{24}$$

Or, because the x-coordinate is defined to be zero at the boundary:

$$\vec{k}_i \cdot \hat{y} + \vec{k}_i \cdot \hat{z} = \vec{k}_r \cdot \hat{y} + \vec{k}_r \cdot \hat{z} = \vec{k}_t \cdot \hat{y} + \vec{k}_t \cdot \hat{z} \tag{25}$$

Equation (25) must be true for all points in the plane where x is defined as zero, allowing two simpler equations to be produced - one when y equals zero and one when z

equals zero:

$$k_i \cdot \hat{y} = k_r \cdot \hat{y} = k_t \cdot \hat{y} \tag{26}$$

$$k_i \cdot \hat{z} = k_r \cdot \hat{z} = k_t \cdot \hat{z} \tag{27}$$

From the above y-equation, and the geometry of Figure 1, the following relation is easily found:

$$k_i \sin\theta_i = k_r \sin\theta_r = k_t \sin\theta_t \tag{28}$$

Substituting the relations between the propagation coefficients k_i, k_r, and k_t (23) into equation (28) produces the following two equations:

$$\theta_i = \theta_r \tag{29}$$

$$\frac{\sin\theta_t}{\sin\theta_i} = \sqrt{\frac{\varepsilon_1\mu_1}{\varepsilon_2\mu_2}} \tag{30}$$

The above equations can be reduced to the familiar form of Snell's Law by defining n, the index of refraction:

$$n = \sqrt{\varepsilon\mu} \tag{31}$$

$$\theta_i = \theta_r \tag{32}$$

$$\frac{\sin\theta_t}{\sin\theta_i} = \frac{n_1}{n_2} \tag{33}$$

The second equation can be solved for θ_t:

$$\theta_t = \sin^{-1}\left(\frac{n_1}{n_2}\sin(\theta_i)\right) \tag{34}$$

Though this is the standard derivation of Snell's law, it leaves one interesting issue unresolved that will prove important later – it is ambiguous whether θ_t should be defined in the +y direction or in the –y direction. This ambiguity can be resolved by examining the normal components on either side of the boundary. The full incident,

reflected, and transmitted field equations are:

$$\vec{E}_i = \vec{E}_{0i} e^{-j\vec{k}_i \cdot \vec{r}} = (E_{oi\_z}\hat{z}) e^{-jk_1(y\sin\theta_i + x\cos\theta_i)} \tag{35}$$

$$\vec{H}_i = \vec{H}_{0i} e^{-j\vec{k}_i \cdot \vec{r}} = (H_{0i\_x}\hat{x} - H_{0i\_y}\hat{y}) e^{-jk_1(y\sin\theta_i + x\cos\theta_i)} \tag{36}$$

$$\vec{E}_r = \vec{E}_{0r} e^{-j\vec{k}_r \cdot \vec{r}} = (E_{or\_z}\hat{z}) e^{-jk_1(y\sin\theta_r - x\cos\theta_r)} \tag{37}$$

$$\vec{H}_r = \vec{H}_{0r} e^{-j\vec{k}_r \cdot \vec{r}} = (H_{0r\_x}\hat{x} + H_{0r\_y}\hat{y}) e^{-jk_1(y\sin\theta_r - x\cos\theta_r)} \tag{38}$$

$$\vec{E}_t = \vec{E}_{0t} e^{-j\vec{k}_t \cdot \vec{r}} = (E_{ot\_z}\hat{z}) e^{-jk_2(y\sin\theta_t + x\cos\theta_t)} \tag{39}$$

$$\vec{H}_t = \vec{H}_{0t} e^{-j\vec{k}_t \cdot \vec{r}} = (H_{0t\_x}\hat{x} - H_{0t\_y}\hat{y}) e^{-jk_2(y\sin\theta_t + x\cos\theta_t)} \tag{40}$$

The boundary conditions for the normal field components include the material properties, via the constitutive relations:

$$\hat{n} \cdot (\vec{B}_1 - \vec{B}_2) = q_{ms} = \hat{n} \cdot (\mu_1 \vec{H}_1 - \mu_2 \vec{H}_2) \tag{41}$$

$$\hat{n} \cdot (\vec{D}_1 - \vec{D}_2) = q_{es} = \hat{n} \cdot (\varepsilon_1 \vec{E}_1 - \varepsilon_2 \vec{E}_2) \tag{42}$$

All electric fields in the three electric field equations are z-directed, so no normal component exists, and no useful relation can be found using the boundary conditions in this case. Applying the magnetic field boundary condition to the three H-field equations, along with the assumption that their surface magnetic charge density is zero, yields a single equation:

$$\mu_1 H_{0i\_x} e^{-jk_1(y\sin\theta_i)} + \mu_1 H_{0r\_x} e^{-jk_1(y\sin\theta_r)} - \mu_2 H_{0t\_x} e^{-jk_2(y\sin\theta_t)} = 0 \tag{43}$$

Once again, because x and y are defined as zero at the boundary, the exponent is eliminated, leaving an equation comprised only of scalar x-directed H-field values:

$$\mu_1 H_{0i\_x} + \mu_1 H_{0r\_x} = \mu_2 H_{0t\_x} \tag{44}$$

Since both permeabilities are positive, and the reflected field normal component must be less than or equal to the incident field normal component due to energy

conservation, the incident field normal component and the transmitted field normal component must have the same sign (the sign of the reflected field depends on which region has greater permeability). Therefore θ_t is in the +y direction.

Now that this method has been developed, it can be used to determine what happens when both μ_2 and ε_2 are negative. From the same scalar x-directed H-field equation, it is evident that because μ_2 and μ_2 have opposite signs, H_{0t_x} and H_{0i_x} must have opposite signs as well. Assuming a similar case where incident, reflected, and transmitted components all keep the same sign (which can be assured by choosing magnitudes of μ_2 and ε_2 relative to μ_1 and ε_1), then negative refraction must occur, as shown in Figure 2. Similar proofs can be derived for when the H-field is in the x-direction, and for arbitrarily directed E-field and H-fields.

For completeness, it would be useful to generalize Snell's law to include the negative angle. For this reason, Veselago [1] proposed a more general version that holds true for both positive and negative refractive indices, with *p* defined by the "handedness" of each material (*p* is +1 for right-handed materials, and -1 for left-handed materials)

$$\frac{\sin\theta_t}{\sin\theta_i} = n_{21} = \frac{p_1}{p_2}\sqrt{\frac{\varepsilon_1\mu_1}{\varepsilon_2\mu_2}} \tag{45}$$

Solving for the transmitted angle:

$$\theta_t = \sin^{-1}\left(\frac{p_1}{p_2}\sqrt{\frac{\varepsilon_1\mu_1}{\varepsilon_2\mu_2}}\sin(\theta_i)\right) \tag{46}$$

In summary, Maxwell's equations allow for electromagnetic propagation in materials with negative permittivity and permeability. The electric field, magnetic field, and propagation vector of a propagating electromagnetic wave in a left-handed material

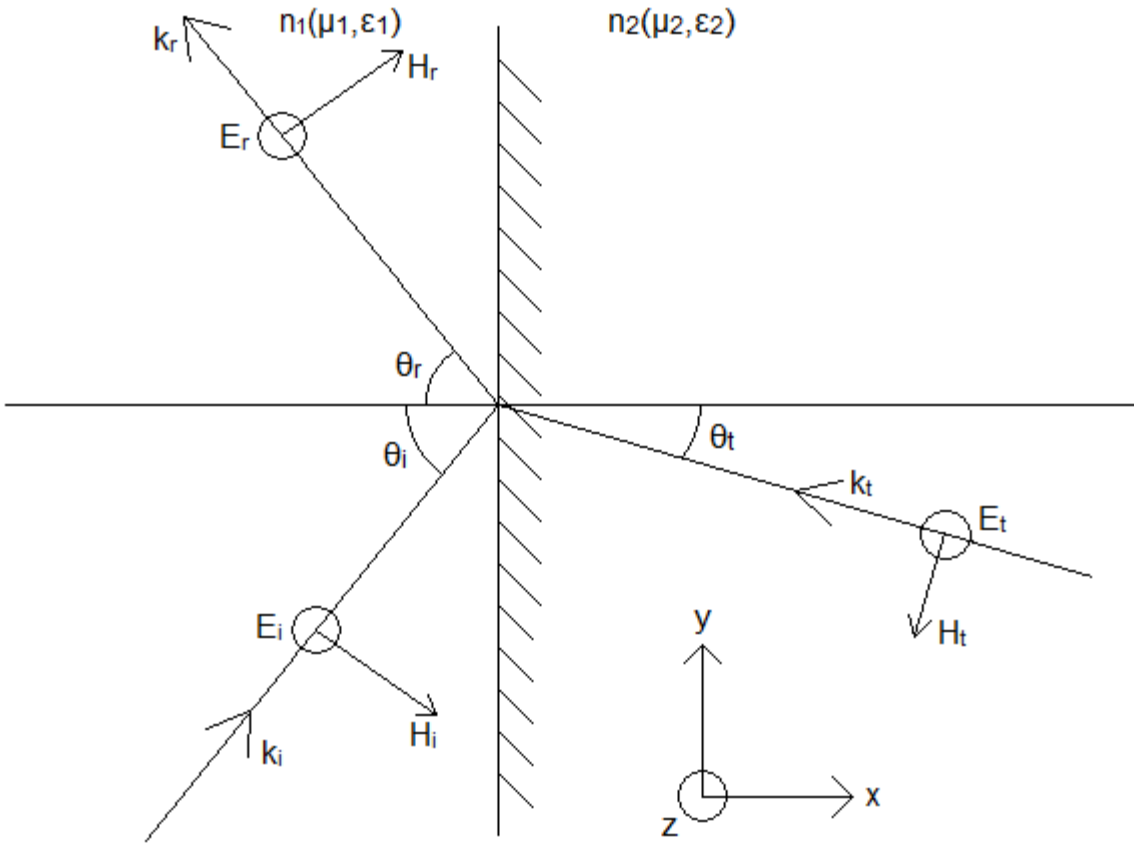

Figure 2: Reflection and refraction at the boundary between PRI and NRI media.

will form a left-hand triplet instead of a right-handed triplet. Because the propagation vector is opposite to the direction of power flow in a left-handed material, phase will propagate in the opposite manner as it does in right-handed materials. Snell's Law can describe boundaries between any combination of traditional materials and left-handed materials with the addition of a "handedness" sign. Accordingly, at a boundary between materials with opposite handedness, the transmitted electromagnetic waves will refract at a negative angle.

2.2 THEORY OF NEGATIVE REFRACTIVE INDEX TRANSMISSION LINES

Left-handed theory can also be used to make a left-handed transmission line (LHTL). Since the only known way of creating a left-handed material uses structures significantly smaller than a wavelength such that an electromagnetic wave sees an aggregate properties rather than individual structures, such materials can be called metamaterials. To derive the properties of a LHTL, it is easiest to start by analyzing a right-handed transmission line (RHTL) of infinitely repeating unit cells.

An ideal RHTL can be modeled as distributed series inductance and resistance, and distributed shunt capacitance and conductance. If divided into sufficiently small cells, each a small fraction of a wavelength, the distributed elements can be treated as lumped elements grouped into unit cells. An example unit cell is shown in Figure 3, with per-length transmission line (TL) cell attributes denoted with an apostrophe.

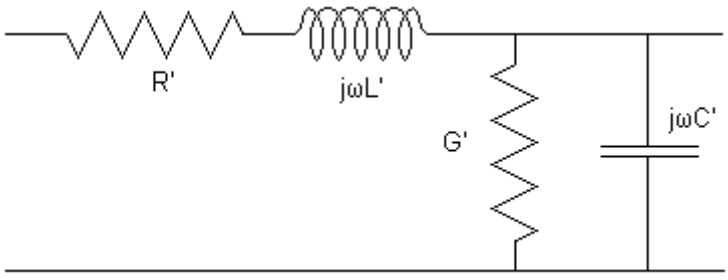

Figure 3: Normal (PRI) transmission line unit cell.

Table 1: Properties of NRI, PRI, unbalanced composite, and balanced composite transmission lines.

	Right-Handed or PRI Cell	Left-Handed or NRI Cell	Unbalanced Composite Cell (negligible resistance)	Balanced Composite Cell (negligible resistance)
Per unit impedance	$R'+j\omega L'$	$\frac{1}{G'+j\omega C'}$	$j\omega L_R'+\frac{1}{j\omega C_L'}$	$j\omega L_R'+\frac{1}{j\omega C_L'}$
Per unit admittance	$G'+j\omega C'$	$\frac{1}{R'+j\omega L'}$	$j\omega C_R'+\frac{1}{j\omega L_L'}$	$j\omega C_R'+\frac{1}{j\omega L_L'}$
Characteristic Impedance	$\sqrt{\frac{R'+j\omega L'}{G'+j\omega C'}}$	$\sqrt{\frac{R'+j\omega L'}{G'+j\omega C'}}$	N/A	N/A
Characteristic Impedance (Negligible Resistance)	$\sqrt{\frac{L'}{C'}}$	$\sqrt{\frac{L'}{C'}}$	$\sqrt{\frac{L_L'(\omega^2 L_R' C_L'-1)}{C_L'(\omega^2 L_L' C_R'-1)}}$	$\sqrt{\frac{L_L'}{C_L'}}=\sqrt{\frac{L_R'}{C_R'}}$
Propagation Coefficient	$\sqrt{(R'+j\omega L')(G'+j\omega C')}$	$\sqrt{\frac{1}{(R'+j\omega L')}\frac{1}{(G'+j\omega C')}}$	N/A	N/A
Propagation Coefficient (Negligible Resistance)	$j\omega\sqrt{L'C'}$	$\frac{1}{j\omega\sqrt{L'C'}}$	$\sqrt{\frac{L_R'}{L_L'}+\frac{C_R'}{C_L'}-\omega^2 C_R' L_R'-\frac{1}{\omega^2 C_L' L_L'}}$	$j\omega\sqrt{C_R' L_R'}+\frac{1}{j\omega\sqrt{C_L' L_L'}}$
Equivalent Free Space Propagation Constant *	$j\omega\sqrt{\varepsilon_R\mu_R}=\frac{j2\pi}{\lambda}$	$\frac{1}{j\omega\sqrt{\varepsilon_L\mu_L}}=-j\frac{\lambda}{2\pi}$	$\sqrt{\frac{\mu_R d}{L_L'}+\frac{\varepsilon_R d}{C_L'}-\omega^2\varepsilon_R\mu_R-\frac{d^2}{\omega^2 C_L' L_L'}}$	$j\omega\sqrt{\varepsilon_R\mu_R}+\frac{d}{j\omega\sqrt{C_L' L_L'}}$
Transition Frequency	N/A	N/A	$\omega_{T1}=\frac{1}{\sqrt{L_L' C_R'}}, \omega_{T2}=\frac{1}{\sqrt{C_L' L_R'}}$	$\frac{1}{\sqrt{C_L' L_L'}}=\frac{1}{\sqrt{C_R' L_R'}}$

* A pure left-handed free space propagation constant is only included for completeness. Unbalanced and balanced composite cell equivalent free space propagation constants assume periodic loading with series capacitive and shunt inductive structures, and unit cell length d.

Using circuit theory, the per unit length impedance and per unit admittance are easily found and are shown in the second column of Table 1. The characteristic impedance and propagation coefficient are also shown in Table 1, along with the simplified forms of each when resistance and conductance are negligible. Finally, demonstrating the similarity between propagation in free space and waveguides, when L' and C' are replaced with ε and μ, the result is the familiar free space propagation constant in the bottom row of Table 1.

Suppose a transmission line were composed of many cells that are the dual circuit of a normal transmission line cell, with shunt inductance and series capacitance, as shown in Figure 4. Such a cell could be called a left-handed cell, many of which would comprise an LHTL. The per unit length impedance and admittance would be the duals of the right-handed cells, as shown in the third column of Table 1. The characteristic impedance of the left-handed cell would still the same. However, the propagation coefficient would be the inverse of the RHTL's propagation constant, and the propagation phase coefficient β (imaginary part of the propagation coefficient) would be the negative reciprocal of the right-handed case, implying reversed direction of phase propagation. The free-space equivalent propagation coefficient (L' and C' and replaced with ε and μ) would also be the inverse of the right-handed case. Thus, if a transmission line could be made of such cells, it would exhibit the same characteristic impedance as a normal transmission line, but with reversed phase propagation.

If a microstrip transmission line were designed to incorporate cells of shunt inductance and series capacitance, it would still contain intrinsic series inductance and

shunt capacitance as well. Therefore, it is important to consider the resulting properties when an RH and an LH cell are combined together in a composite transmission line (CTL), as shown in Figure 5. For simplicity, conductance and resistance are neglected.

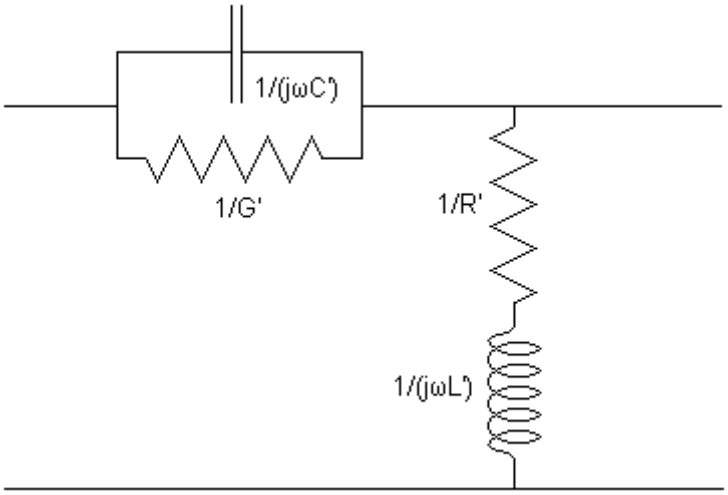

Figure 4: Ideal NRI transmission line unit cell.

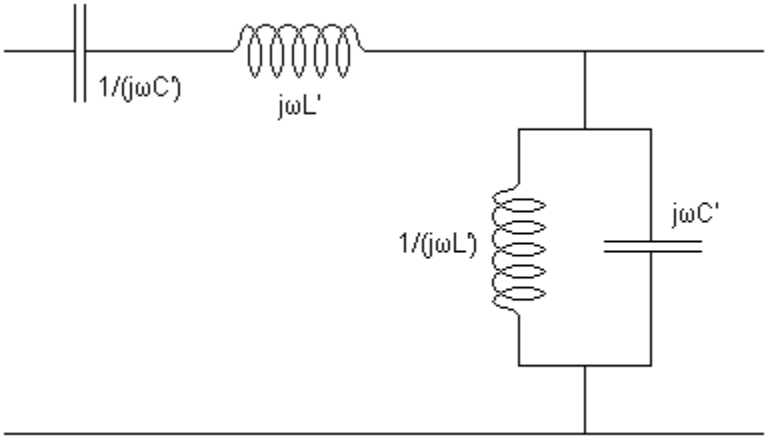

Figure 5: Composite transmission line unit cell.

As shown in Table 1, the per length impedance and per length admittance of a CTL are simply the sums of the RH and LH cells. The per-length characteristic impedance and propagation coefficient become much more complicated, and only the "negligible resistance" case is shown in the fourth column of Table 1. Interestingly, the characteristic impedance can be separated into the impedance of the LH section, and a composite term comprised of all four per-length properties.

A special case of the CTL results when the inductances and capacitances are related as follows:

$$L_R'C_L' = L_L'C_R' \tag{47}$$

When this relationship exists, the characteristic impedance simplifies to the same as both the LH and RH cases in Table 1. Meanwhile, the propagation coefficient simplifies to the sum of the LH and RH propagation coefficients. This condition is referred to in literature as the "balanced" condition [12].

A useful tool for analyzing propagation characteristics is the dispersion diagram, which shows how the propagation coefficient β varies as a function of frequency. Both phase velocity and group velocity can be easily seen on a dispersion diagram, since phase velocity is frequency divided by β, and group velocity is the derivative of phase velocity. In the upper left graph of Figure 6, a conventional TL dispersion diagram is shown with phase velocity and group velocity both independent of frequency, as well as in the same direction (same sign). In an LHTL (upper right), the propagation coefficient is negative and increases asymptotically towards zero as frequency increases. Group velocity is positive, but phase velocity is negative, which demonstrates left-handed

propagation. In a balanced CTL (lower left), the propagation coefficient asymptotically approaches that of the conventional TL propagation coefficient with increasing frequency, and asymptotically approaches that of LHTL propagation coefficient with decreasing frequency. While group velocity is always positive, phase velocity changes sign at a transition frequency related to the material per-unit properties (see Table 1). This transition frequency is the points at which left-handed behavior reverts back to right-handed behavior. Finally, an Unbalanced CTL (lower right), has similar performance to a balanced TL, but with the addition of a stopband between a pair of transition frequencies (also shown in Table 1).

By loading a normal transmission line with repeating shunt inductance and series impedance at intervals significantly smaller than a wavelength, a composite transmission line can be made. At frequencies below the transition frequency or band, left-handed behavior will dominate and phase advances backwards. At frequencies above, right-handed behavior will dominate and phase propagates normally. If the loading is chosen to satisfy the balanced condition, no stopband exists between the left-hand and right-hand regions. The existence of left-handed transmission lines in which phase propagates backwards should allow for many novel devices, especially when combined with normal transmission line segments. Even more generally, with four independent parameters available in a composite transmission line, it should be possible to independently control characteristic impedance and the propagation coefficient in both the left-hand and right-hand regions.

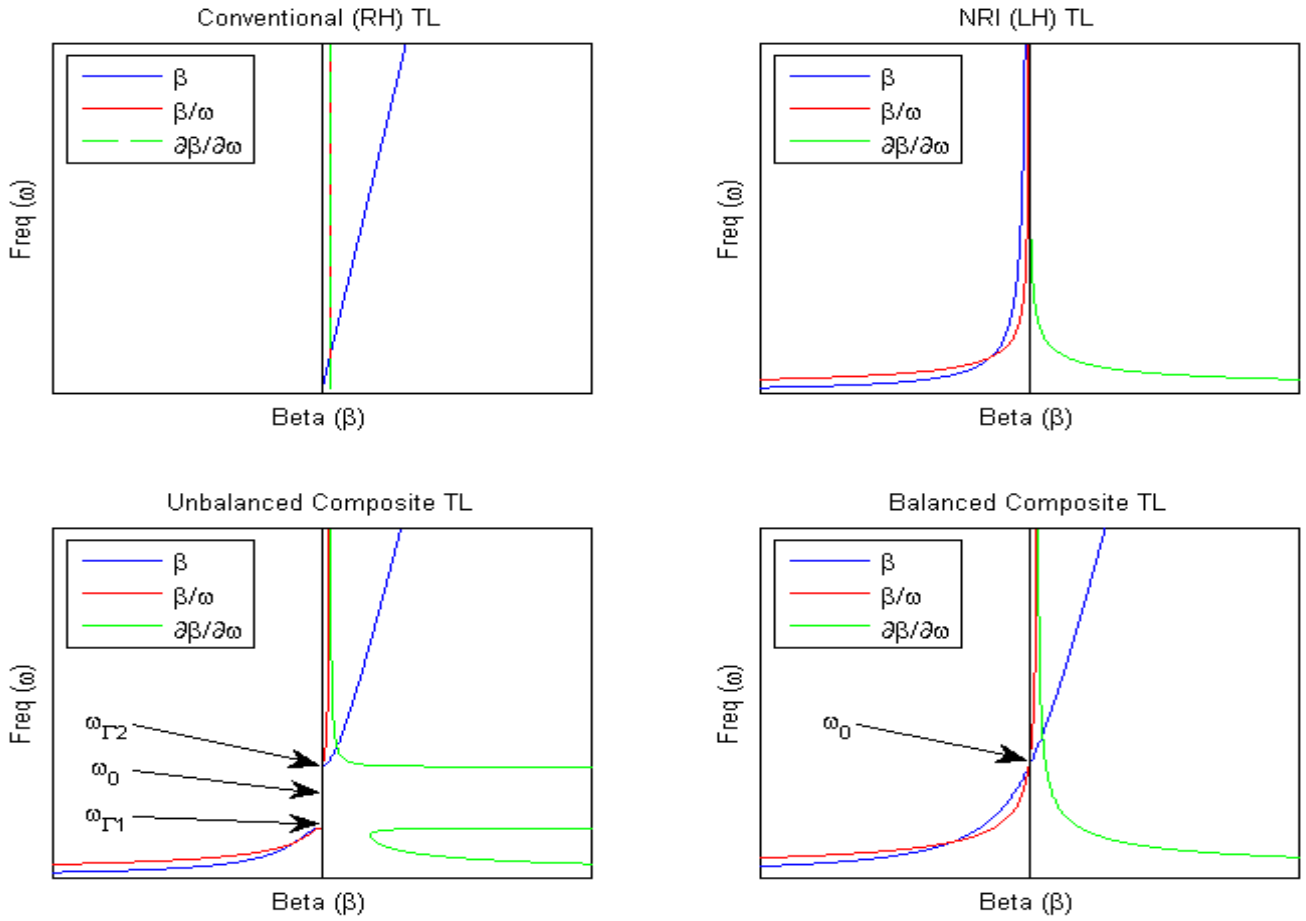

Figure 6: Dispersion diagrams for conventional, left-handed, balanced composite, and unbalanced composite TLs.

3. NEGATIVE REFRACTIVE INDEX LITERATURE REVIEW

3.1 ORIGIN AND DEVELOPMENT OF NEGATIVE REFRACTIVE INDEX MEDIA

Veselago's groundbreaking original paper [1] discussed the theoretical properties of any material with simultaneously negative permittivity and permeability. He was not able to synthesize such a material; he only predicted its properties based on the study of fundamental equations. The only fundamental equations where permittivity and permeability appear separate, rather than as a product, are Maxwell's equations and the constituent equations. From these equations, Veselago derived that propagation in left-handed materials would keep the same Poynting vector (direction of energy transfer) as propagation in right-handed materials, but that the phase would propagate in the opposite direction. In addition, he concluded that the Doppler Effect would be reversed and that the Cerenkov Effect would result in photons being emitted at an angle towards the source rather than at an angle away from the source. Veselago also predicted that Snell's Law should be changed to allow for transitions between materials of different "rightness" - while the reflected wave is unchanged, the refracted wave should be reflected across the axis perpendicular to the transition place, exhibiting a negative refractive index. For what Veselago calls "Fresnel's formulas," which calculate transmission and reflection amplitudes as a function of incident angle, "rightness" does not matter, as the formulas only use the product of ε and μ. Using his updated version of Snell's Law, Veselago predicted that convex left-handed lenses would be diverging, that concave left-handed lenses would be converging, and that any left-handed material must

be dispersive (ε and μ must be a function of frequency and not constant). Finally, Veselago discussed the possibility of gyrotropic materials demonstrating a negative refractive index and speculated that if magnetic monopoles were possible, their presence would be mostly hidden by a tendency of the monopoles to concentrate. One questionable conclusion that troubled Veselago is that existing physics, combined with his derived left-handed material properties, would result in light pressure (caused by photon momentum) exerting an attractive rather than repulsive force on a reflecting body in a left-handed media.

In 1962, Rotman published a paper detailing how to simulate the effects of reentry plasma and rocket exhaust on antennas and radar reflections [3]. Since plasma should have a permittivity whose real part is negative, Rotman created two artificial dielectrics with negative permittivity – one using periodically spaced metallic rods and one using periodically spaced parallel plates. Rotman's parallel plates were only usable for 2D simulations, but the metallic rods could be used for 1D, 2D, and 3D cases. At the time, fabrication techniques limited the parallel rod media to sub-microwave frequencies therefore most of Rotman's work involved the parallel plate method. Nonetheless, Rotman was able to demonstrate negative permittivity using a metallic rod lattice with spacing $<0.2\lambda$, as well as derive its transmission line equivalent circuits.

Over 30 years after Rotman published his simulation of plasma effects using metallic rods, Pendry et al. researched plasmon phenomena at extremely low frequencies [4]. Previously, surface plasmon phenomena (oscillations in surface electrons of a metal which cause most metals to appear shiny) had only been seen at visible light and UV

frequencies, but Pendry et al. demonstrated plasmons and negative permittivity at 6-12GHz using a 3D grid of metallic wires [5]. They also thoroughly investigated the conditions and properties of the media, including the importance of interconnections between orthogonal wires and the limits of isotropic behavior. Due to the difference in application between plasma simulation and plasmon phenomena, as well as Rotman's predominant focus on parallel plates, Pendry et al. was apparently unaware of Rotman's work with similar metallic rod grids over 30 years earlier.

A year later, in 1999, Pendry et al. developed 1D, 2D, and 3D grids of split rings that demonstrated negative permeability [6]. Their proposed split ring structures were made of thin metal sheets which he proposed could comprise the faces of cubic building blocks. Pendry et al. derived the mathematical performance of various types of split rings, their isotropic behavior in a 3D grid, and potential nonlinear effects. They even mentioned that the split ring structure could be combined with a metallic grid structure to enable both negative permittivity and custom permeability.

Though Pendry et al. suggested combining metallic grids and split rings for generalized custom materials, it was Smith et al. in 2000 who connected the potential of these techniques to actually implement Veselago's proposed left-hand material, as well as correctly attributing Rotman with the original formulation of the negative permittivity metallic grid structure [7]. Their paper detailed both simulation and construction of a 2D media which exhibited simultaneous negative permeability and negative permittivity.

A year later in 2001, Shelby et al. built a 2D prism out of the same metallic grid and split ring structure with unit cells that were ~1/6 wavelength, measured the

refraction angle at X-band, and calculated that it corresponded to an index of refraction of -2.7±0.1 [8]. The authors noted that left-handed materials tend to be highly dispersive and acknowledged measurement limitations that prevent them from measuring regions where the magnitude of the index of refraction is greater than 3, or when the index of refraction is imaginary. Finally, while discussing whether negative refraction is possible at optical frequencies, the authors noted that the existence of surface waves and operation above the Bragg reflection frequency will make it very difficult to verify negative refractive metamaterials at optical frequencies.

Almost 40 years after his original paper and two years after Shelby et al. first demonstrated negative refraction, Veselago followed up on their demonstration with a new paper containing restatements and new conclusions [13]. He pointed out that materials with negative ε and μ are still lossy, i.e., the sign of the imaginary components ε" and μ" remains positive. He also reiterated that Snell's law is still true, that convex and concave lenses would reverse their properties, and that Cerenkov radiation would be produced towards the source rather than away. Veselago pointed out that being able to create materials with arbitrary ε and μ is far more useful than just creating a material with negative ε and μ – such custom materials can be used for impedance matching to prevent reflections/refractions at boundaries, for example. He also said that Fermat's principle should not be interpreted in terms of propagation time, but rather in terms of optical length, where optical length is negative in a negative refractive index material. Finally, he questioned whether isotropic 3D materials with negative refractive indices are possible, saying this was still unknown.

Pendry followed up his previous papers with an article [14] discussing the feasibility of "superlenses" - lenses capable of focusing light onto an area smaller than a square wavelength. Using causal math, Pendry proved that a left-handed material is capable of amplifying evanescent waves, and argued this is still causal because evanescent waves do not transport energy. Next, Pendry discussed how a thin sheet of silver can be used as a lossy superlens. Finally, Pendry proposed using his split ring structure for imaging inside nonmagnetic objects using focusing of magnetic fields at GHz frequencies.

Veselago Pendry, and Smith have also published corrections concerning two misinterpretations about NRI work. The first was caught by Pendry and Smith in 2006; they explained unusual interference patterns in NRI materials and confirmed that both group and phase velocity are reversed in left-handed materials [15]. The second was Veselago's rebuttal [16] of Pendry et al. and others who implied that NRI lenses can amplify evanescent modes, thereby imaging objects smaller than a wavelength and acting as a "superlens". Veselago pointed out that such a result would violate the uncertainty principle, which can be stated as below:

$$k_x d \geq 2\pi \tag{48}$$

By combining the uncertainty principle with the definition of the free space propagation coefficient (49), a relationship between wavelength and minimum resolution size can be found:

$$k_x < k_0 = \frac{\omega}{c} = \frac{2\pi}{\lambda} \tag{49}$$

$$d \geq \lambda \tag{50}$$

The inequality in (50) prohibits amplifying objects smaller than a wavelength. Veselago also argued that because the flat "lens" described by Pendry is less than a wavelength thick, and the distances to object and image planes is of similar distance, it is actually a matching device rather than a lens. Matching devices are capable of concentrating energy into cross-sectional areas smaller than a wavelength (e.g., waveguide detectors use screws or slots to focus energy on the detector), but do not function at distances significantly greater than a single wavelength. A lens, on the other hand, is thicker than a wavelength and operates at distances greater than a wavelength. All proposed NRI "superlenses" published before 2005 have used thicknesses and distances of less than a wavelength and Veselago stated they therefore should not be considered lenses.

Luo et al. avoided the above controversy by ignoring possible evanescent fields and mathematically examined "thick" left-handed slabs (thickness greater than a wavelength) [17]. By using the paraxial model for laser beams, they showed that a perfect image plane exists on the far side of a left-handed slab, provided that the slab thickness is equal to the sum of the distances between the object plane and the slab, and between the image plane and slab. The slab's refractive index must also be the negative of the refractive index in the regions on either side of the slab. A perfect image plane

also would exist halfway through the negative refractive index slab. Since this was primarily an optical analysis, they also derived that a negative refractive index will cause a negative Rayleigh length and inverse Gouy phase shift in left-handed materials.

Though practical implementations of negative refractive index materials have existed for less than a decade, their properties were predicted almost 50 years ago. The predicted properties include negative refraction, reversed phase propagation, high dispersion, and reversal of lens behavior. Reversed Doppler Effect and reverse direction of Cherenkov radiation were also predicted, but have not been proven experimentally at this time. More negative refractive index properties are still being theoretically debated, including resulting direction of force applied by light pressure and amplification of evanescent fields. Whether or not negative refractive index materials are possible at optical frequencies, they can be built at microwave frequencies, and have great potential for novel ways of implementing filters and other microwave circuits.

3.2 TYPES OF NEGATIVE REFRACTIVE INDEX MEDIA

As previously discussed, the basic theory of negative refractive index materials can be simply stated as creating negative permeability and negative permittivity using repeating structures. Such negative properties must be large enough to dominate over the inherent material or free space properties in a frequency band [18]. In a transmission line, the equivalent of negative permeability and negative permittivity is series capacitance and shunt inductance.

For one-dimensional NRI transmission lines, several techniques can be used to create series capacitance and shunt inductance. In 2002, a group led by Eleftheriades demonstrated a negative refractive index antenna using coplanar waveguide with capacitive gaps and inductive thin lines [19]. A year later, they demonstrated both a transmission line [20] and a series of phase shifters using coplanar waveguide with series chip capacitors and shunt chip inductors [21]. Meanwhile, the same year a group led by Caloz and Itoh demonstrated several devices including an antenna and three different types of couplers that used microstrip transmission lines with interdigital capacitors and inductive stubs shorted to ground with vias [22]. To date, the remaining method used for 1D NRI transmission lines is microstrip with series chip capacitors and chip inductors shunted to ground with vias. Scher et al. at Texas A&M University published the first 1D application – a microstrip resonator [9]. Each method has inherent advantages and disadvantages: methods using discrete chips are limited by the available values and Q factors of the chips, but can create very compact circuits due to the relatively small size of chip inductors and capacitors. Methods using microstrip or coplanar waveguide structures are generally larger due to etching limitations, but can be used for arbitrary values of capacitance and inductance. Finally, while microstrip

circuits require vias, coplanar waveguide circuits do not.

Smith et al. published the first 2D NRI material using a grid of split ring resonators and wire inductors [7]. This material was difficult to fabricate, since it consisted of many small circuit boards oriented perpendicular to the plane of propagation. Nonetheless, they successfully demonstrated negative refraction with this arrangement [8]. Eleftheriades et al. published the first planar 2D NRI structure in 2002, after he realized that resonators are not required for NRI properties. They developed a structure consisting of microstrip transmission lines with chip capacitors and chip inductors with vias [23]. Surprisingly, this 2D application preceded nearly identical one-dimensional microstrip methods. Meanwhile in 1999 Sievenpiper et al. discovered and studied a periodic "mushroom" structure with unusual properties, including both a forbidden band for surface propagation and reflection of incident waves without phase reversal [24]. In 2004, Sanada et al. postulated that this "mushroom" structure's capacitive plates and shunt vias possessed NRI properties, and demonstrated negative refraction and focusing using a stripline version of the structure [25].

Though researchers had found several different 1D and 2D NRI structures, 3D structures eluded them until Alitalo et al. published a microstrip-based 3D NRI media in 2006 [26]. Each 2D layer of their NRI media consisted of a grid of microstrip with series chip capacitors and shunt chip inductors. Vertically-oriented microstrip boards containing series capacitors served as interconnects between three 2D layers. Alitalo et al. reported approximately isotropic behavior, as well as backward phase propagation and amplification of evanescent modes. A year later, Zedler et al. proposed a fully 3D

matrix of cells with interior inductive wires and exterior capacitive metal plates for each cell [27]. A circuit simulation of a 3D matrix of cells demonstrated both two NRI frequency bands and the ability to support orthogonal polarizations in any direction. Zedler et al. then constructed a single unit cell and confirmed that it closely matched the behavior seen in a circuit simulation of a single cell. To date, while other 3D NRI structures have been proposed for microwave frequencies, no others have been experimentally verified.

In the last decade various researchers have experimentally verified one, two, and three dimensional NRI materials at microwave frequencies. One-dimensional NRI materials are the most mature, with many different fabrication techniques and types of transmission lines. Several groups have developed two dimensional NRI materials and successfully demonstrated NRI focusing and negative refraction. Three dimensional methods of producing a negative refractive index remain the most immature of all, as only two limited versions have been built and tested.

3.3 NOVEL CIRCUITS DEVELOPED WITH NEGATIVE REFRACTIVE INDEX TRANSMISSION LINES

NRI transmission lines possess two particularly useful properties for microstrip circuits – negative phase propagation and inherent dual-band behavior with sufficient degrees of freedom to tune behavior in both frequency bands. A variety of resonators, filters, couplers, phase shifters, power dividers, and antennas have been developed and demonstrated using NRI transmission lines. Unfortunately, many exhibit both excessive loss and an unpredictable frequency shift between design and fabrication. A few that are claimed to be NRI circuits are arguably better explained as normal transmission line circuits that use both shunt inductance and series capacitance.

Three groups reported on NRI resonators between 2003 and 2005. Sanada et al. built a resonator consisting solely of an NRI cell made from two interdigital capacitors and a shunt stub inductor [28]. They reported an unloaded Q of 250 and showed that the resonant frequency is mostly independent of the resonator length. While the authors note that the resonance is caused by the shunt inductive stub and the NRI cell's shunt capacitance (series inductance and shunt capacitance are inherent properties of transmission lines), they fail to note that this might better be explained as a simple shunt resonator. Scher et al. used chip capacitors and chip inductors for the NRI cell with normal transmission line segments on either side [9]. Since the electrical length of the NRI cell is equal to the sum of the two normal transmission line segments, resonant behavior is caused by a total phase length of zero degrees, making this a true zeroth order resonator. At the resonator's resonant frequency of 1.2 GHz, the chip inductor

limited the unloaded Q of the resonator to about 48. Unlike a normal resonator (including that of [28]), no higher-order harmonics occur because the NRI cell only exhibits negative phase propagation below a transition frequency deliberately positioned under what would otherwise have been the first harmonic frequency. A year later, Salehi and Mansour reported a similar coplanar waveguide zero order resonator constructed from interdigital capacitors and shunt meander line inductors that exhibited an unloaded Q of about 30 at 2.3 GHz [10].

A variety of groups have proposed filters based on NRI transmission lines, but before discussing their results, it is instructive to consider the differences between filters and NRI media, as the two can be confused. Caloz and Itoh report three major differences [29]:

(1) Filters are generally designed only to meet magnitude responses; the CRLH cells of a NRI transmission line are designed to meet specific phase responses.

(2) The CRLH cells of NRI transmission lines and media must satisfy a homogeneity condition of unit cell electrical length less than one quarter wavelength to be seen as a homogeneous material; filters generally do not have this condition.

(3) Filters are 1D; NRI media can be 1D, 2D, or even 3D.

In the same publication as their coplanar waveguide zeroth order resonator, Salehi et al. also reported a coplanar waveguide three pole filter made from PRI and NRI cells [10]. Similar to the filter reported in the results section of this thesis, they discovered significant differences between simulation and measured results: the insertion losses increased from less than 0.5dB to greater than 3dB, the center frequency shifted

from 2.8 GHz (HFSS) to 2.6 GHz, and the upper rejection band began fading at a frequency about 30-60% higher than the center frequency. A year later, Li et al. published a paper postulating the use of notch filters made from alternating sections of right and left-handed transmission lines [30]. Based on ADS simulations, they show notch filters with a 2.2% stopband bandwidth at 900 MHz, with anywhere from 19.2dB to 68.1dB rejection, and only 0.045dB passband loss. However, these filters required 20-60 unit cells (depending on stopband rejection) and used only ideal inductors and capacitors.

In 2005 Wei et al published a general method of constructing NRI filters [31]. Their method consists of starting with a highpass filter, transforming to a bandpass filter, and using K-inverters in order to create a microstrip design that could be realized using only series interdigital capacitors, shunt inductive stubs, and capacitance to ground. However, applying transforms to a filter until it consists of interdigital capacitors and shunt stub inductors does not mean it consists of left-handed or NRI elements. When Caloz's and Itoh's guidelines [29] are applied, this filter fails to meet two criteria: no specific phase response is required in the cells and it is not required to meet the homogeneity condition. Instead, this filter is best explained as a filter comprised of four coupled shunt resonators.

Couplers are perhaps the most promising types of circuits developed using NRI transmission lines. Caloz et al. demonstrated a backwards coupled-line coupler consisting of two coupled NRI transmission lines [32],[33]. The coupler is "backwards" because the NRI lines couple phase in the opposite direction, resulting in the coupled

port being adjacent to the input port rather than diagonal from it. A second frequency band below the NRI band exhibited excellent through performance without coupling; the authors attribute this to magnetic coupling. At the higher band, the coupled level was only 0.6dB below the input level; at the lower band the through level was about 1dB below the input level. They concluded that a coupler made from CRLH cells can be both smaller than a conventional coupled-line coupler and have a much larger gap between the coupled lines while still providing a higher coupling level. Caloz and Itoh then created a coupled-line coupler out of one NRI line and one normal transmission line [34]. This coupler also exhibited very high coupling levels, dual-band behavior, a 2dB bandwidth greater than 50%, and an even smaller size than the dual NRI coupled-line couplers.

In addition to coupled-line couplers, novel branch-line and hybrid ring couplers can also be made using NRI transmission lines. Islam and Eleftheriades simulated and constructed two types of 1.1 GHz branch-line couplers using a mix of conventional and left-handed transmission lines – one with left-handed lines replacing the high impedance lines and one with left-handed lines replacing the low impedance lines [35]. Both exhibited a zero-degree phase shift at the coupled port, rather than the -180 degrees of a conventional design. At the through port, one exhibited a -90 degree phase shift like a conventional branch-line coupler, and the other +90 degree phase shift. In addition to providing performance that was comparable to conventional branch-line couplers, these NRI couplers were also smaller. Lastly, Islam and Eleftheriades proposed that combinations of these two couplers and conventional branch-line couplers could provide

any desired mix of 0, +90, -90, and 180 degrees of phase at the four output ports of a hybrid-based power divider. Caloz and Itoh placed NRI cells in all four arms of a branch-line coupler, and found that careful selection of series capacitance and shunt inductance allowed for not only dual-band operation, but also arbitrary selection of the two frequencies [22]. In the same publication, they also reported a hybrid ring coupler that used a -90 degree CTL in place of the 270 degree transmission line, resulting in both reduced size and a 54% increase in bandwidth.

Two more novel applications of NRI TLs are phase shifters and series power dividers. Eleftheriades and Antoniades developed a series of lead-lag phase shifters in which proper adjustment of the series capacitance and shunt inductance can create any phase delay while maintaining the impedance match [21]. In addition, this type of phase shifter exhibits less group delay, customizable phase shift as a function of frequency, and smaller size than conventional phase shifters. The same researchers also produced a broadband series power divider composed of four zero phase length transmission lines, each with a physical length of one-eighth wavelength [36]. Each zero phase length line is comprised of a 30 degree normal transmission line and a -30 degree NRI transmission line together designed not to radiate. Both the metamaterial and a conventional power divider showed 0.8-0.9dB average losses, but the metamaterial power divider had 50-60% wider bandwidth and occupied much less space than the conventional series power divider, at the cost of a ~0.2dB higher insertion loss.

NRI materials and transmission lines can even be used to make antennas and arrays. In 2002, Eleftheriades and Grbic published a backwards wave antenna [37].

Their antenna used a 16-cell NRI structure in coplanar waveguide, with each cell about one fifth of a free space wavelength in length, and with higher phase velocity than free space. This requires a refractive index that is both negative and smaller than free space's in magnitude. The authors claim that their antenna is the first to operate in the "long wavelength regime", unlike slow wave structures that radiate a non-fundamental spatial harmonic, or log-periodic structures that are half-wavelength structures and do not have effectively negative permeability and permittivity. The prototype antenna produced a -38.5 degrees backwards-directed mainlobe at 14.6 GHz, implying a -0.623 refractive index. As the frequency was increased, the beam scanned towards broadside, consistent with the end of the negative refractive index region. The same year, Liu et al. created a backfire-to-endfire linear array composed of 24 composite transmission line cells [38]. As frequency was swept from 3.4 to 4.3 GHz, the array scanned from 32 degrees to -15 degrees, with efficiency greater than 40%. By design, the array was steered to broadside at the transition frequency of the composite cells.

The various NRI circuits discussed previously can be combined into even more complex circuits. In March 2009 Abdalla et al. created a four element, 2.4 GHz series-fed phased array with NRI/PRI phase shifters [39]. Conventional series-fed phased arrays require 360 degree shifts between elements resulting in longer trace lengths and frequency-based scan angle squint. In addition, they can only be scanned to one side of broadside unless the input and termination ports are swappable. NRI/PRI phase shifters allow the phase shift between elements to be varied to both positive and negative phase, allowing the beam to steer to either side of broadside. NRI/PRI phase shifters also have

small size and short group delay, which together address the remaining two shortcomings of conventional series-fed phased arrays. For the phased array in [39], the NRI cells were composed of varactors and tunable active inductors, allowing for constant impedance of the NRI cell as the phase shifter was varied across its 197 degree range. As the varactor bias voltage was varied, the array scanned from -27 to 22 degrees, the mainbeam gain ranged from 6.9 to 8.4dBi with sidelobes always at least 10dB down, and halfpower beamwidth varied between 25 degrees (boresight) and 29 degrees (max scan). Since the array used non-linear devices, it exhibited a 1dB compression point at 4.5dBm output, and a third order intermodulation intercept point of 8.8dBm. One downside of this array the authors did not discuss was the need for nine power and control lines per phase shifter for the active components.

Perhaps the most powerful aspect of NRI transmission lines is the addition of both an additional degree of freedom and the ability to independently set two frequencies of operation. Lin et al. applied these principles to a quarter wavelength CTL and found that the CTL can provide +/- 90 degree electrical length at two independent frequencies [40]. More generally, they found that deliberate selection of the four CTL parameters can place any desired pair of phases at any two frequencies. Such capability should allow for wider bandwidth circuits, dual-frequency capability, and novel designs in the future.

4. NEGATIVE REFRACTIVE INDEX TUNABLE FILTER RESULTS

To test the feasibility of creating a tunable filter using combined positive refractive index and negative refractive index (PRI/NRI) techniques, models of the desired filter topology were built in several simulators. Microwave Studio was used to make a 2-pole bandpass filter centered at 1.5 GHz. The substrate, line lengths, line widths, and lumped element values were chosen to provide both a clear filter characteristic and to minimize filter size. Since Microwave Studio uses formula approximations for microstrip layout shapes, it simulates quickly enough to allow for real time tuning of parameters with immediate viewing of results. The same design was recreated in Zeland IE3D to test phase sensitivity using the 2.5D simulator and ideal lumped elements. Using IE3D ensured that the shape approximations used in Microwave Studio were consistent with a more accurate method-of-moments simulation. Finally, Agilent ADS was used to compare a filter with ideal lumped elements to a filter with vendor-provided models of lumped elements. Agilent ADS is capable of both formula approximations and method-of-moments. While Microwave Studio, Zeland IE3D, and both modes of Agilent ADS all agreed when ideal lumped elements were simulated, Agilent ADS provided significantly differently results when using the vendor models for the varactors, chip capacitors, and wire-wound inductors.

Figure 7 shows the general layout of the proposed NRI filter topology, and Figure 8 shows a photo of the physical circuit. An Agilent ADS layout for simulating the PRI/NRI filter with vendor models of lumped elements compared with the later

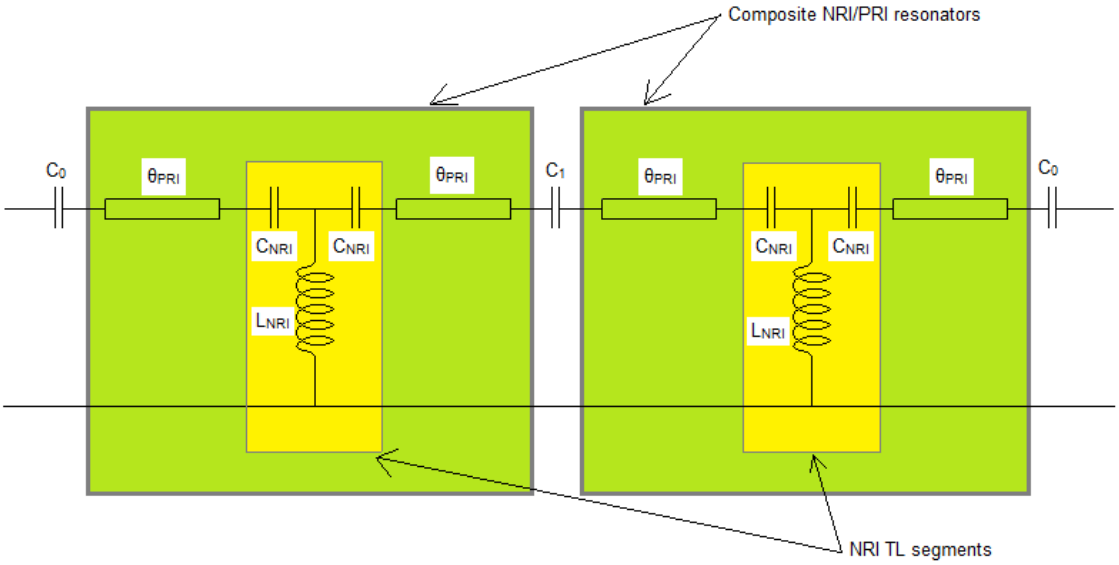

Figure 7: Proposed filter layout schematic.

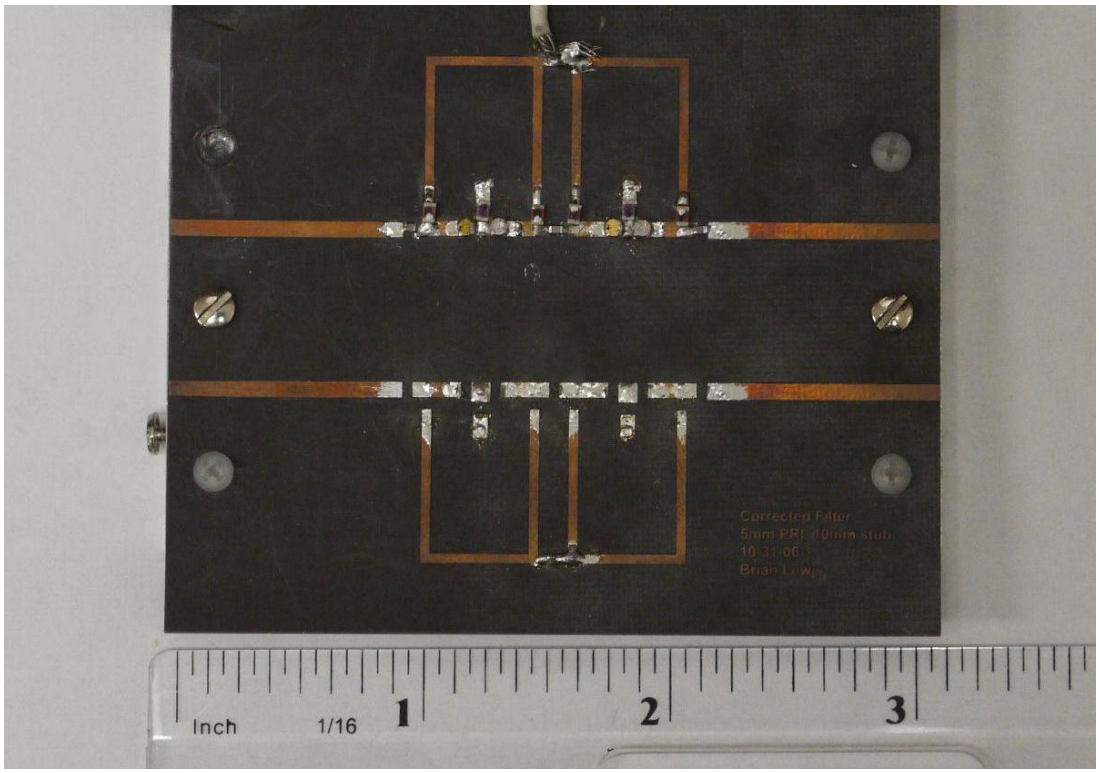

Figure 8: Physical layout of the tunable two-resonator filter.

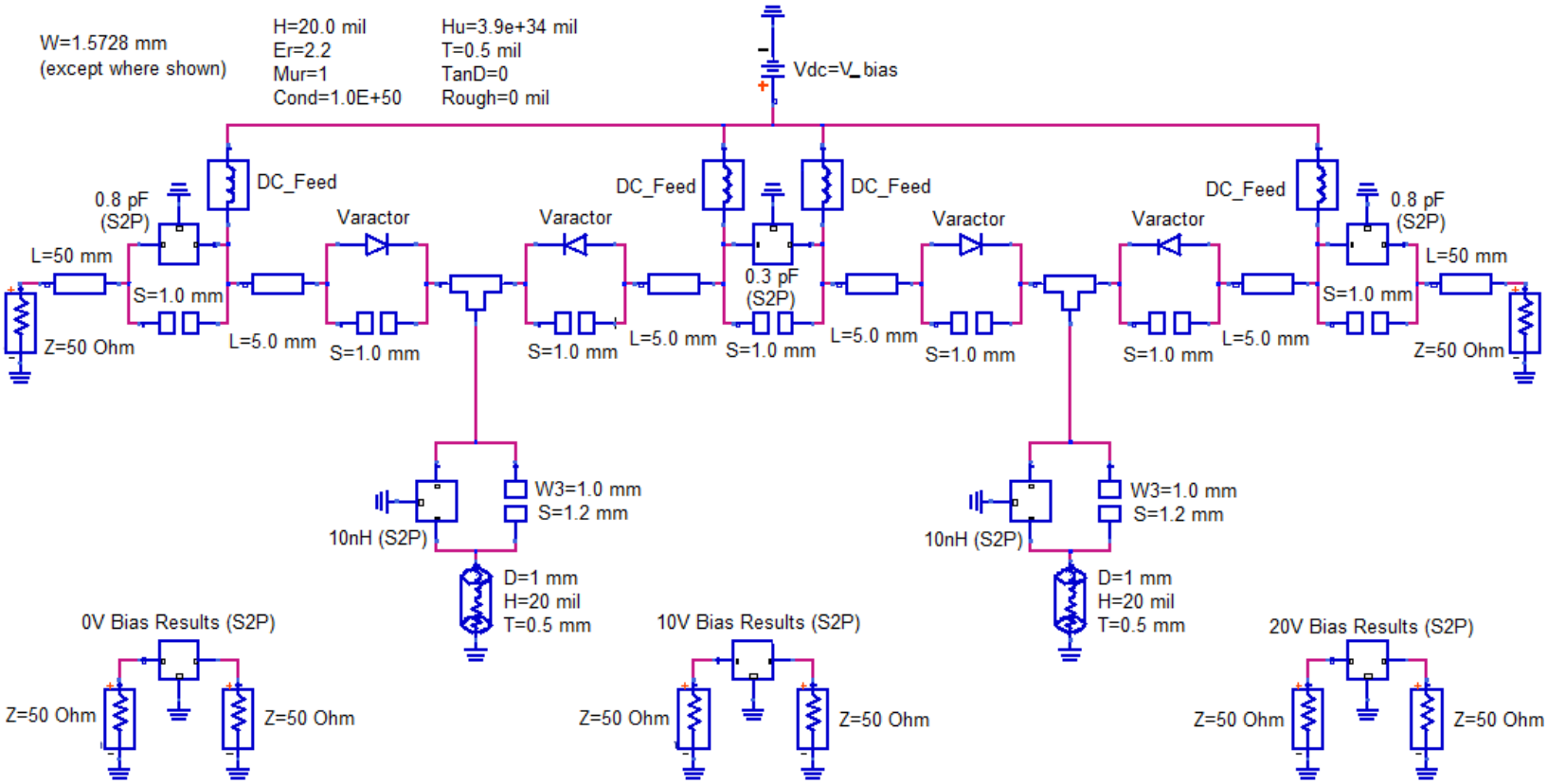

Figure 9: ADS simulator layout for comparing filter simulations using vendor models with filter measurements.

measured results is shown in Figure 9. While the wire-wound inductors and chip capacitors had S-parameter models from the vendors, only a Spice model was available from the varactor vendor. Figure 10 compares the 10nH shunt inductance filter design with ideal elements in ADS to measured results. A frequency shift of approximately 10% occurred between ideal simulation and measurement, likely due to the parasitic effects of the lumped elements and inherent capacitance between the NRI TL soldering areas and the ground plane, neither of which is included in the ideal simulation.

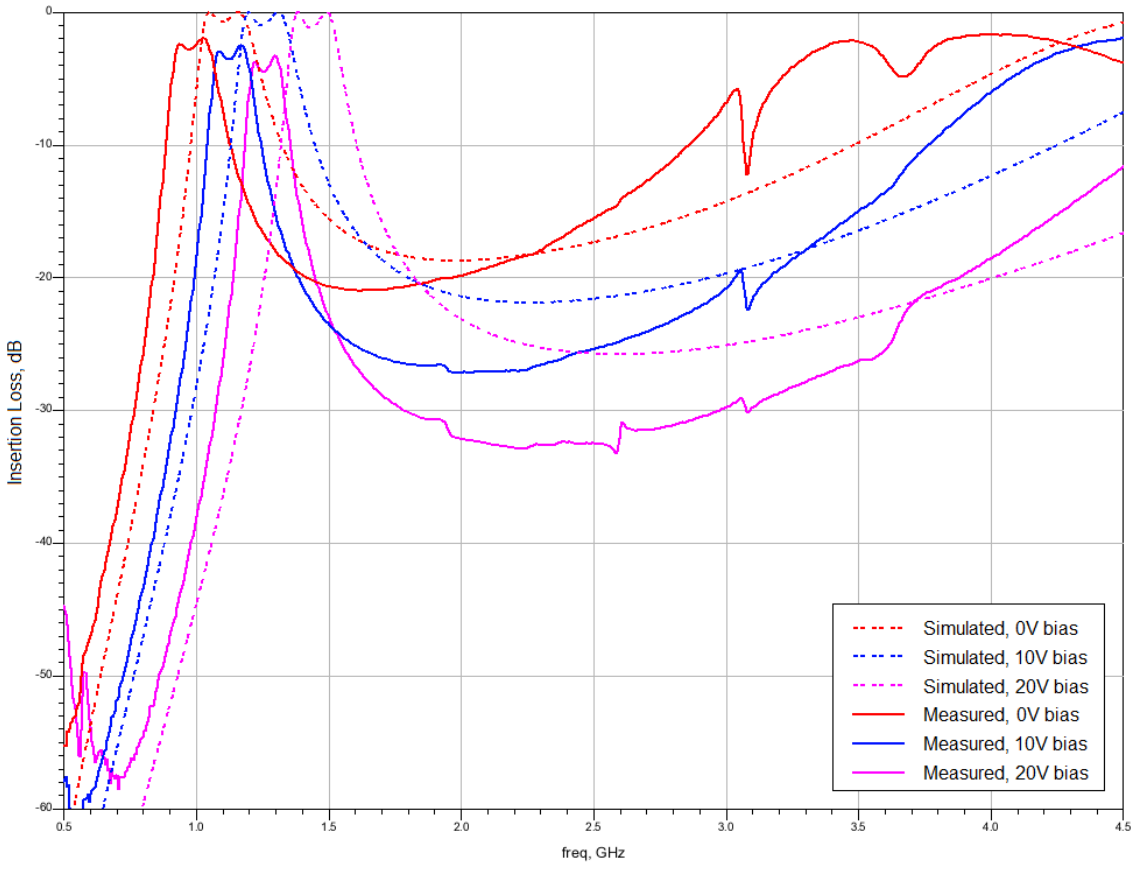

Figure 10: Simulation with ideal lumped elements vs. measured results of first NRI filter layout with 10nH shunt inductors, and 0.8pF and 0.3pF series capacitors.

Figure 11 compares measured results to an ADS model incorporating vendor-supplied lumped elements models (see Appendix A for additional results). In addition to the results shown in Figures 10 and 11, three other design variations were simulated. All four designs use 0.3pF coupling capacitors on each side of the filter, and a 0.8pF coupling capacitor between the resonators. The four designs differ in the shunt inductance: 4.7nH, 6.8nH, 8.2nH, or 10nH. Each design was measured at bias voltages of 0V, 10V, and 20V, at which each varactor produced a capacitance of 10pF, 2.3pF, and1.0pF, respectively, making the filter tunable by varying the bias voltage.

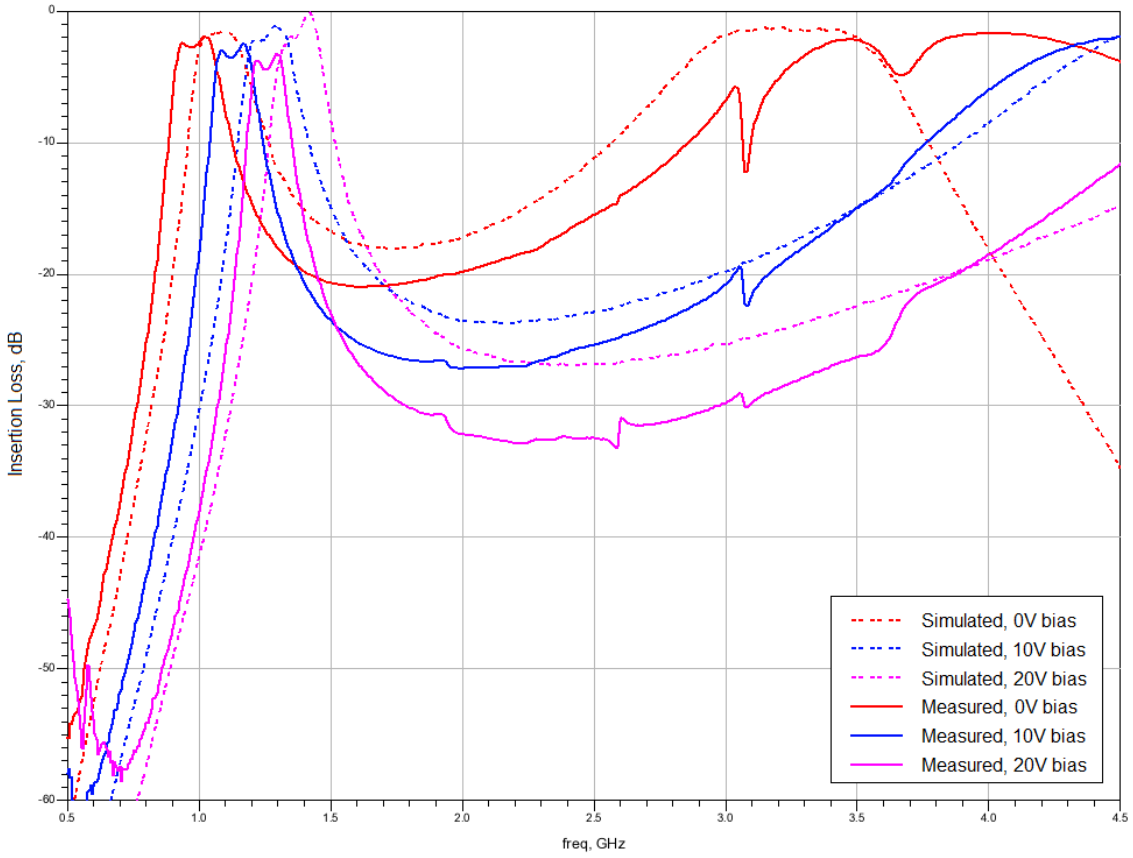

Figure 11: Simulation with vendor supplied models vs. measured results of first NRI filter layout with 10nH shunt inductors, and 0.8pF and 0.3pF series capacitors.

After initial simulations, various prototypes were constructed. All prototypes were created on Duroid 5880 using wet etching. Vias were machined with a drill press using a 1mm drill bit and filled using oven-cured conductive epoxy. All designs used M/A-COM MA46H203 varactors to make the filter tunable. Initially, the physical circuits used chip inductors for shunt inductances and RF chokes, wide line widths on thick substrate, and interdigital capacitors for series capacitances. These characteristics were subsequently changed. Chip inductors could not provide sufficient inductance at 1.5 GHz, as evidenced by sensitivity to touching the biasing wires from the power supply. Subsequent attempts showed that either Coilcraft 0805HT wire-wound inductors or inductive shunt stubs could provide the proper inductance for RF chokes and shunt inductors. The final boards used wire-wound inductors for the added ability to adjust inductor values without etching a new board. Similarly, since interdigital capacitors required a new board etching for any change in value, final boards used 0603 chip capacitors from Johanson Technology. Finally, the wide line widths and thick substrate were replaced with 1.57mm line widths on 20mil substrate to decrease the filter size once interdigital capacitors were no longer being used.

After all of the above revisions were incorporated, two board layouts were fabricated. Both used 5mm line length for the Positive Refractive Index (PRI) sections of the resonators. The first circuit layout was tested with four values of shunt inductance as described previously, but had a 0.8mm minor error in gap sizes for the shunt inductors and little room for soldering at common nodes. This led to difficulty soldering lumped elements because some gaps were wider than the inductor contacts and required solder to

bridge the excess gaps, and difficulty soldering contacts for two varactors and one inductor to the same small common node. The second circuit layout had corrected gap sizes and 1mm more room to solder at the common nodes, and was tested with multiple combinations of coupling capacitances, as well as two values of shunt inductance. Full results for both layouts are shown in the Appendix A. Both designs used M/A-COM MA46H203 varactors, Johanson Technology 0603 chip capacitors, Coilcraft 0805HT inductors, and 5mm PRI microstrip line lengths.

After fabrication and measurement, the results were compared with the ideal element simulations (Figure 10 and Appendix A). The measured results exhibited a 10% downward shift in resonant frequency, a 2-4dB increase in insertion loss, and distortion of the passband when compared with the ideal simulated results. The insertion loss increase was related to the tuning frequency – at the lowest frequency (lowest bias voltage) the insertion loss increased by 2dB, and increased nearly linearly to 4dB at the highest frequency. The simulations were repeated using Spice models provided by the vendors. Simulated and measured results matched more closely, with a smaller frequency shift and better insertion loss agreement (Figure 11 and Appendix A). While the simulation with Spice models exhibited some distortion in the passband, primarily at the highest bias voltage, the distortion was still different from the measured results. Since the varactors produce their minimum capacitances at the highest bias voltage, differences in the parasitic effects between vendor models and circuit simulations should be most apparent at the higher tuning frequencies. These parasitic affects likely caused the passband distortions in the measurements. Passband shape and insertion loss at low

varactor biasing (high varactor capacitance and low tuning frequency) were more consistent between simulation and physical measurement.

The remaining small frequency shift between simulation and measurement was likely due to inaccuracies in the simulations of effective transmission line length – filters made from PRI and NRI segments are extremely sensitive to transmission line length. A 1mm error in effective line length causes only a 1% frequency shift in a half-wavelength 1.2 GHz resonator (91mm in length), but because a 10 degree 1.2 GHz long PRI microstrip line is only 5mm long, a 1mm error will cause a frequency shift eighteen times larger due to the length of the PRI line changing by 20%. Such frequency shifts and increases in insertion loss are common in NRI devices [20].

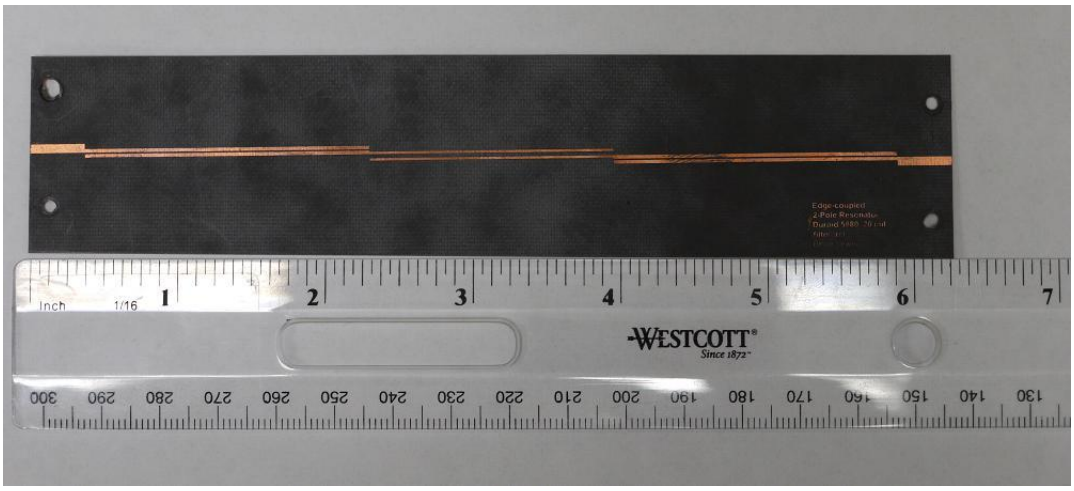

Figure 12: Conventional 1.25GHz two-resonator coupled-line filter.

In order to compare the PRI/NRI filters with a conventional filter, a standard two- resonator 1.25GHz coupled-line filter was designed and constructed using the same

substrate and substrate thickness as the NRI filters (Figure 12). The line widths, line thicknesses, and gap sizes were optimized using Zeland IE3D for minimum insertion loss at the desired frequency. The resulting filter was approximately 5 inches long. In comparison, the tunable PRI/NRI double resonator filter was 1.25 inches long, or a 4x decrease in size.

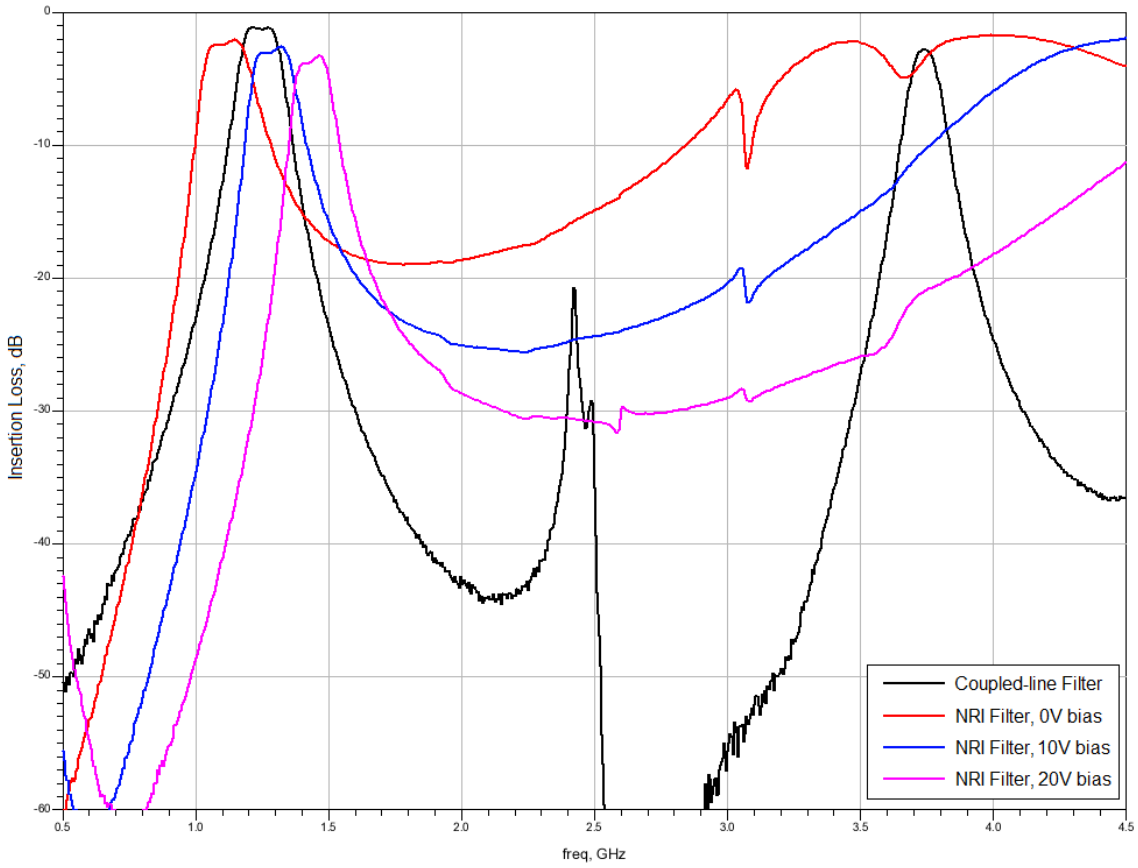

Figure 13: Comparison of coupled-line resonator with first NRI filter layout using 8.2nH shunt inductors, and 0.8pF and 0.3pF series capacitors.

When compared, the classic coupled-line resonator and tunable NRI resonator had similar passband widths and center frequencies (Figure 13), but also showed several

key differences:

1) While the coupled-line filter displayed multiple resonant frequencies (at 4x, 8x, etc. of the design frequency), the NRI filter did not, because well-designed NRI resonators do not exhibit higher resonances [9]. Instead, its rejection decayed with increasing frequency, due to fading NRI properties and the limited SRF of the lumped elements. The rate of lessening of the rejection was a function of the tuning frequency with the best rejection (and slowest decay of the rejection) at the highest bias voltage and highest tuning frequency.
2) The NRI filter exhibited higher insertion loss than the conventional filter. Its insertion loss also increased with the tuning frequency.
3) The coupled line filter demonstrated better rejection above the passband.
4) The conventional filter was much better matched to 50 Ohms. The NRI filter showed input mismatch, especially at higher tuning frequencies (Figure 14).

Tabulated results for all circuits are shown in Table 2, and all results are graphed in the Appendix A. Overall, insertion loss varies from 2-3dB, tuning bandwidth was around 25%, and center frequencies ranged from 990-1827 MHz. Various passband shapes were demonstrated, including no ripple, 0.5dB ripple, and 3dB ripple.

The primary issue with this NRI filter topology is that input impedance could not be controlled across the filter tuning range. Since only the NRI series capacitance was tunable and not the NRI shunt inductance, input impedance shifted as a function of varactor capacitance (Figure 14), causing the circuit to be mismatched at high bias voltage (low varactor capacitance). A second issue is that the Self-Resonant Frequency

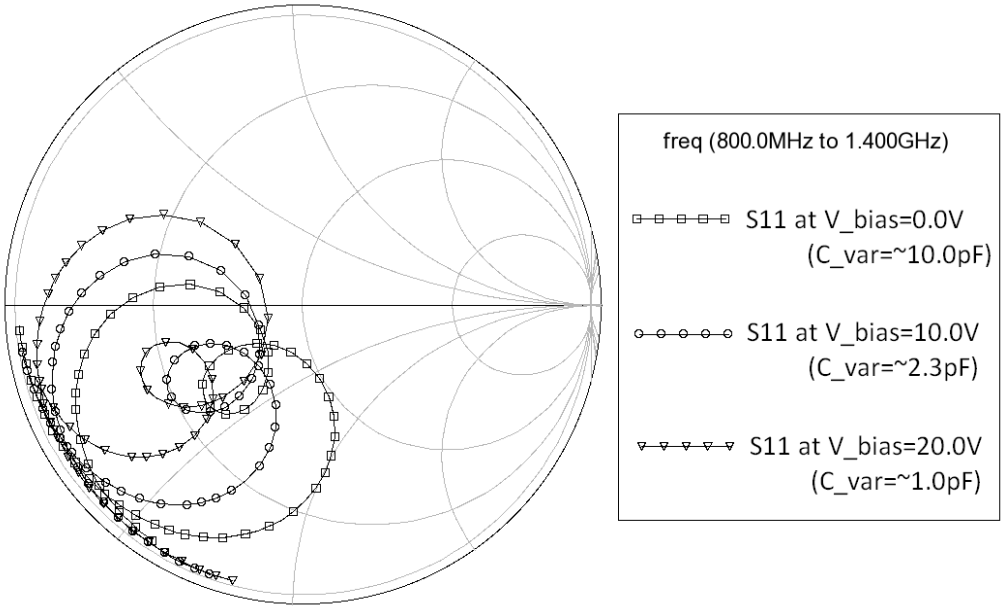

Figure 14: Smith chart of S11 of tunable NRI filter with 10nH shunt inductance, and 0.3pF and 0.8pF series capacitance.

(SRF) of the chip inductors limited the frequency scaling of the bandpass filter design.

The SRF of the 0805HT chip inductors ranged from 3300 MHz to 5500 MHz; above the SRF, the chip inductors no longer provide inductance. Also, the Q factor of the Coilcraft 0805 HT inductors at 1250 MHz ranged between 80 and 100, and faded with increasing frequency. Inductors that retain their inductance at higher frequencies and have a much higher SRF, such as inductive shunt stubs, should significantly help the filter response and scaling to higher frequencies.

In summary, these results show that filters can be designed using composite PRI/NRI techniques. These filters are significantly smaller than filters made from 180 degree microstrip resonators, and can be made tunable by replacing series capacitors

Table 2: Tabulated results from all circuits and layouts.

						Center Frequency			3dB Bandwidth			Insertion Loss			Ripple Depth			Ripple Bandwidth			
						0V	10V	20V	0V	10V	20V	0V	10V	20V	0V	10V	20V	0V	10V	20V	
L_NRI	C_0	C_1	PRI	NRI	Layout	10pF	2.3pF	1pF	10pF	2.3pF	1pF	10pF	2.3pF	1pF	10pF	2.3pF	1pF	10pF	2.3pF	1pF	Tuning BW
(nH)	(pF)	(pF)	(mm)	(mm)		(MHz)	(MHz)	(MHz)	(MHz)	(MHz)	(MHz)	(dB)	(dB)	(dB)	(dB)	(dB)	(dB)	(MHz)	(MHz)	(MHz)	
10.0	0.8	0.3	10	3	1st	990	1133	1263	162	142	132	1.942	2.481	3.265	0.87	1.09	1.21	125	120	110	24.23%
8.2	0.8	0.3	10	3	1st	1118	1290	1440	180	154	142	2.068	2.595	3.268	0.45	0.50	0.58	105	100	85	25.18%
6.8	0.8	0.3	10	3	1st	1182	1360	1513	196	164	145	1.900	2.349	2.830	0.37	N/A	N/A	100	N/A	N/A	24.56%
4.7	0.8	0.3	10	3	1st	1398	1625	1821	241	208	207	1.694	2.204	3.400	N/A	N/A	N/A	N/A	N/A	N/A	26.28%
4.7	0.8	0.3	10	4	2nd	1362	1598	1788	212	180	169	1.840	2.286	2.757	N/A	N/A	0.17	N/A	N/A	80	27.05%
4.7	0.8	0.5	10	4	2nd	1323	1561	1783	342	265	233	1.614	2.035	2.501	2.90	2.17	1.67	340	260	205	29.62%
4.7	0.8	0.15	10	4	2nd	1384	1617	1821	116	119	110	4.213	4.024	4.454	N/A	N/A	N/A	N/A	N/A	N/A	27.27%
4.7	1.0	0.15	10	4	2nd	1323	1583	1798	180	146	129	7.567	5.988	5.790	N/A	N/A	N/A	N/A	N/A	N/A	30.44%
4.7	1.0	0.5	10	4	2nd	1283	1534	1759	336	266	234	1.270	1.599	2.018	N/A	0.59	0.46	N/A	170	140	31.30%
4.7	1.0	0.3	10	4	2nd	1307	1562	1780	202	199	178	2.428	2.268	2.642	N/A	N/A	N/A	N/A	N/A	N/A	30.64%
4.7	0.5	0.3	10	4	2nd	1406	1628	1827	225	182	174	2.322	2.904	3.570	1.90	1.57	1.21	210	180	145	26.04%
10.0	0.8	0.3	10	4	2nd	984	1137	1273	154	132	112	1.826	2.328	2.937	0.38	0.56	0.53	90	95	80	25.61%
Standard Parallel-Coupled Filter						1244			160			1.141			0.15			90			N/A

with properly biased varactors. Fundamentally, the performance of this design is limited by the SRF and Q factor of the elements used. At higher frequencies, the Q factor of lumped elements inherently decreases, with three impacts on the filter:

1) Increase in passband insertion loss
2) Decrease in filter rolloff slope
3) Decrease in rejection

These effects could be mitigated by choosing better performing lumped elements, or switching some lumped elements to higher Q microstrip elements that can be tuned with lumped elements.

Future versions of this filter design could use independently tunable shunt inductances to keep transmission line segment impedance constant, with the added benefits of allowing tuning of the circuit after fabrication to compensate for unexpected parasitic effects. Control of both shunt inductance and series impedance would also allow for control of filter shape for larger filters (Chebychev, Butterworth, Elliptical, etc.). As an alternative to tunable shunt inductances, varactors could be placed on the inductive shunts.

5. CONCLUSIONS

5.1 SUMMARY

Negative refractive index (or left-handed) media possess several useful properties, including negative refraction, high dispersion, and negative phase propagation. A negative refractive transmission line can be created by using repetitive structures that create series capacitance and shunt inductance at intervals a small fraction of the wavelength. The resulting composite transmission line is capable of dual-band operation, with independent control of transmission line impedance and propagation coefficient in each band. A short NRI transmission line in series with a short normal transmission line creates a resonant structure with zero phase length. Like any resonant structure, these zeroth order resonators can be used to create a filter.

In this thesis, a family of tunable bandpass filters was successfully constructed using end-coupled zeroth order resonators. Tuning was accomplished by controlling the negative phase length of the NRI section by replacing the series capacitors with varactors. The resulting L-band filters exhibited a 25-40% tunable range, 2-4dB insertion loss, and required only one fourth the length of a filter constructed from traditional 180 degree microstrip resonators. Like zeroth order resonators, the NRI filter exhibited no higher order resonances, but its rejection above the passband does fade as the NRI segment's properties decreased with increasing frequency. Overall, the results show that NRI-based tunable filters have potential for any application that requires a compact tunable filter.

5.2 RECOMMENDATIONS FOR FURTHER RESEARCH

Two major improvements could be made to the filters presented in this thesis. First, because the shunt chip inductors were not tunable, the filter input impedance shifted as the series varactors were adjusted, causing insertion loss to increase with frequency. This problem could be reduced or eliminated by using tunable active inductors (if nonlinear response and custom fabrication are acceptable) or varactors in series with the shunt inductors. Second, the Q factor of the chip inductors limited the Q factor of the filter. Higher Q chip inductors or microstrip inductive shunt stubs could significantly improve the filter performance.

Zeroth order resonators could be used in many types of filters. Parallel-coupled microstrip filters could potentially benefit both from the enhanced coupling seen from NRI transmission lines [32]-[34] and the absence of higher order resonant modes in zeroth order resonators [9],[10]. Just as varactor-based zeroth order resonators allowed for frequency tuning of end-coupled resonator-based filters in this thesis, they could also be used for frequency tuning of parallel-coupled line filters.

The use of varactors rather than interdigital capacitors or chip capacitors in NRI circuits could lead to novel couplers. In [32]-[34], coupled-line couplers that incorporate NRI transmission lines are presented. Substituting varactors could allow control of the coupled and through level, or control of the transition frequency between the coupled band and the through band.

REFERENCES

[1] V.G. Veselago, "The electrodynamics of substances with simultaneously negative values of ε and μ," *Sov. Phy.—Usp.*, vol. 10, no. 4, pp. 509-514, Jan.-Feb. 1968.

[2] A.K. Iyer and G.V. Eleftheriades, "Negative refractive index transmission line metamaterials," in *Negative-Refraction Metamaterials*, G.V. Eleftheriades and K.G. Balmain, Eds., Hoboken, NJ: Wiley, 2005, pp. 1-52.

[3] W. Rotman, "Plasma simulation by artificial dielectrics and parallel-plate media," *IEEE Trans. Antennas Propag.*, vol. AP-10, no. 1, pp. 82-95, Jan. 1962.

[4] J. B. Pendry, A. J. Holden, W. J. Stewart and I. Youngs, "Extremely low frequency plasmons in metallic meso structures," *Phys. Rev. Lett*., vol. 76, pp. 4773-4776, Jun. 1996.

[5] J. B. Pendry, A. J. Holden, D. J. Robbins and W. J. Stewart, "Low frequency plasmons in thin wire structures," *J. Phys. [Condensed Matter]*, vol. 10, pp. 4785-4809, Jun. 1998.

[6] J. B. Pendry, A. J. Holden, D. J. Robbins and W. J. Stewart, "Magnetism from conductors and enhanced nonlinear phenomena," *IEEE Trans. Microw. Theory Tech.*, vol. 47, no. 11, pp. 2075-2084, Nov. 1999.

[7] D. R. Smith, W. J. Padilla, D. C. Vier, S. C. Nemat-Nasser and S. Schultz, "Composite medium with simultaneously negative permeability and permittivity," *Phys. Rev. Lett.*, vol. 84, no. 18, pp. 4184-4187, May 2000.

[8] R. A. Shelby, D. R. Smith and S. Shultz, "Experimental verification of a negative

refractive index of refraction," *Science*, vol. 292, no. 5514, pp. 77-79, Apr. 2001.

[9] A.D. Scher, C.T. Rodenbeck and K. Chang. "Compact gap coupled resonator using negative refractive index microstrip line," *Elec. Lett.*, vol. 40, no. 2, pp. 126-127, Jan. 2004.

[10] H. Salehi and R.R. Mansour, "A novel quasi lumped-element resonator using a left-handed transmission line section," in *IEEE MTT-S Int. Microw. Symp. Dig.*, Long Beach, CA, 2005, pp. 1475-1478.

[11] D.J Griffiths, *Introduction to Electrodynamics*, 3rd ed. Upper Saddle River, NJ: Prentice-Hall, 1999.

[12] A. Lai, T. Itoh and C. Caloz. "Composite right/left-handed transmission line metamaterials," *IEEE Microw. Mag.*, vol. 5, no. 3, pp. 34-50, Sept. 2004.

[13] V.G. Veselago, "Electrodynamics of media with simultaneously negative electric permittivity and magnetic permeability," in *Advances in Electromagnetics of Complex Media and Metamaterials*, S. Zouhdi, A. H. Sihvola, and M. Arsalane, Eds., Norwell, MA: Kluwer Academic Publishers, 2002, pp.83-97.

[14] J. B. Pendry, "Negative refraction makes a perfect lens," *Phys. Rev. Lett.*, vol. 85, no. 10, pp. 3966-3939, Oct. 2000.

[15] J.B. Pendry and D.R. Smith, "Comment on "Wave Refraction in Negative-Index Media: Always Positive and Very Inhomogeneous," *Phys. Rev. Lett.*, vol. 90, no.2, article 029703, Jan. 2003.

[16] V.G. Veselago. "Some remarks regarding electrodynamics of materials with negative refraction," *Appl. Phys. B*, vol. 81, pp. 403-407, Jul. 2005.

[17] H. Luo, W. Hu, Z. Ren, W. Shu and F. Li, "Focusing and phase compensation of paraxial beams by a left-handed material slab," *Opt. Comm.*, vol. 266, no. 1, pp. 327-331, Oct. 2006.

[18] G. V. Eleftheriades, O. Siddiqui and A. K. Iyer, "Transmission line models for negative refractive index media and associated implementations without excess resonators," *IEEE Microw. Wireless Compon. Lett.*, vol. 13, no. 2, pp. 51-53, Feb. 2003.

[19] A. Grbic and G. V. Eleftheriades, "Experimental verification of backward-wave radiation from a negative refractive index metamaterial," *J. Appl. Phys.*, vol. 92, no. 10, pp. 5930-5935, Nov. 2002.

[20] O. Siddiqui, M. Mojahedi and G. V. Eleftheriades, "Periodically loaded transmission line with effective negative refractive index and negative group velocity," *IEEE Trans. Antennas Propag*., vol. 51, no. 10, pp. 2619-2625, Oct. 2003.

[21] M. A. Antoniades and G. V. Eleftheriades, "Compact linear lead/lag metamaterial phase shifters for broadband applications," *IEEE Antennas Wireless Propag. Lett.*, vol. 2, pp. 103-106, 2003.

[22] C. Caloz and T. Itoh, "Novel microwave devices and structures based on the transmission line approach of meta-materials," in *IEEE MTT-S Int. Microw. Symp. Dig*., Philadelphia, PA, 2003, vol. 1, pp. 195-198.

[23] G.V. Eleftheriades, A. K Iyer and P. C. Kremer, "Planar negative refractive index media using periodically L-C loaded transmission lines," *IEEE Trans. Microw.*

Theory Tech., vol. 50, no. 12, pp. 2702-2712, Dec. 2002.

[24] D. Sievenpiper, L. Zhang, R. F. J. Broas, N. G. Alexópolous, E. Yablonovitch, "High-impedance electromagnetic surfaces with a forbidden frequency band," *IEEE Trans. Microw. Theory Tech.*, vol. 47, no. 11, pp. 2059-2074, Nov. 1999.

[25] A. Sanada, C. Caloz, and T. Itoh, "Planar distributed structures with negative refractive index," *IEEE Trans. Microw. Theory Tech.*, vol. 52, no. 4, pp. 1252-1263, Apr. 2004.

[26] P. Alitalo, S. Maslovski, and S. Tretyakov, "Experimental verification of the key properties of a three-dimensional isotropic transmission-line superlens," *J. Appl. Phys.*, vol. 99, no. 12, pp. 124910-1-124910-6, Jun. 2006.

[27] M. Zedler, C. Caloz, and P. Russer, "A 3-D isotropic left-handed metamaterial based on the rotated transmission-line matrix (TLM) scheme," *IEEE Trans. Microw. Theory Tech.*, vol. 55, no. 12, pp. 2930-2941, Dec. 2007.

[28] A. Sanada, C. Caloz, and T. Itoh, "Novel zeroth-order resonance in composite right/left-handed transmission line resonators," in *Proc. Asia-Pacific Microw. Conf.*, Seoul, South Korea, 2003, vol. 3, pp. 1588-1591.

[29] C. Caloz and T. Itoh, *Electromagnetic Metamaterials: Transmission Line Theory and Microwave Applications.* Hoboken, NJ: Wiley, 2006.

[30] J.S. Li, B. Chen, J. Yao, Y.Z. Zou, J.D. Hu and S. He, "A novel notch filter utilizing a composite right/left-handed transmission line," *Microw. Opt. Tech. Lett.*, vol. 48, no. 3, pp. 626-628, Mar. 2006.

[31] L. Wei, Q. Zhu Z. Jianfang, and X. Shanjia, "Design of bandpass filter with left-

handed transmission line and highpass prototype," in *Proc. Asia-Pacific Microw. Conf.*, Suzhou, China, 2005, pp. 1419-1421.

[32] C. Caloz, A. Sanada, L. Liu and T. Itoh, "A broadband left-handed (LH) coupled-line backward coupler with arbitrary coupling level," in *IEEE MTT-S Int. Microw. Symp. Dig*., Philadelphia, PA, 2003, vol. 1, pp. 317-320.

[33] C. Caloz, A. Sanada, L. Liu and T. Itoh, "A novel composite right-/left-handed coupled-line directional coupler with arbitrary coupling level and broad bandwidth," *IEEE Trans. Microw. Theory Tech.*, vol. 52, no. 3, pp. 980-992, Mar. 2004.

[34] C. Caloz and T. Itoh, "A novel mixed conventional microstrip and composite right/left-handed backward-wave directional coupler with broadband and tight coupling characteristics," *IEEE Microw. Wireless Compon. Lett.*, vol. 14, no. 1, pp. 31-33, Jan. 2004.

[35] R. Islam and G. V. Eleftheriades, "Phase-agile branch-line couplers using metamaterial lines," *IEEE Microw. Wireless Compon. Lett.*. vol. 14, no. 7, pp. 340-342, Jul. 2004.

[36] M. A. Antoniades and G. V. Eleftheriades, "A broadband series power divider using zero-degree metamaterial phase shifting lines," *IEEE Microw. Wireless Compon. Lett.*. vol. 15, no. 11, pp. 808-810, Nov. 2005.

[37] A. Grbic and G. V. Eleftheriades, "Experimental verification of backward-wave radiation from a negative refractive index metamaterial," *J. Appl. Phys.*, vol. 92, no. 10, pp. 5930-5935, Nov. 2005.

[38] L. Lui, C. Caloz, and T. Itoh, “Dominant mode leaky-wave antenna with backfire-to-endfire scanning capability,” *Electron. Lett,* vol. 38, no. 23, pp. 1414-1416, Nov. 2002.

[39] M. A. Y. Abdalla, K. Phang, and G. V. Eleftheriades, “A planar electronically steerable patch array using tunable PRI/NRI phase shifters,” *IEEE Trans. Microw. Theory Tech.*, vol. 57, no. 3, pp. 531-541, Mar. 2009.

[40] I. Lin, M. DeVincentis, C. Caloz, and T. Itoh, “Arbitrary dual-band components using composite right/left-handed transmission lines,” *IEEE Trans. Microw. Theory Tech.*, vol. 52, no. 4, pp. 1142–1149, Apr. 2004.

APPENDIX A

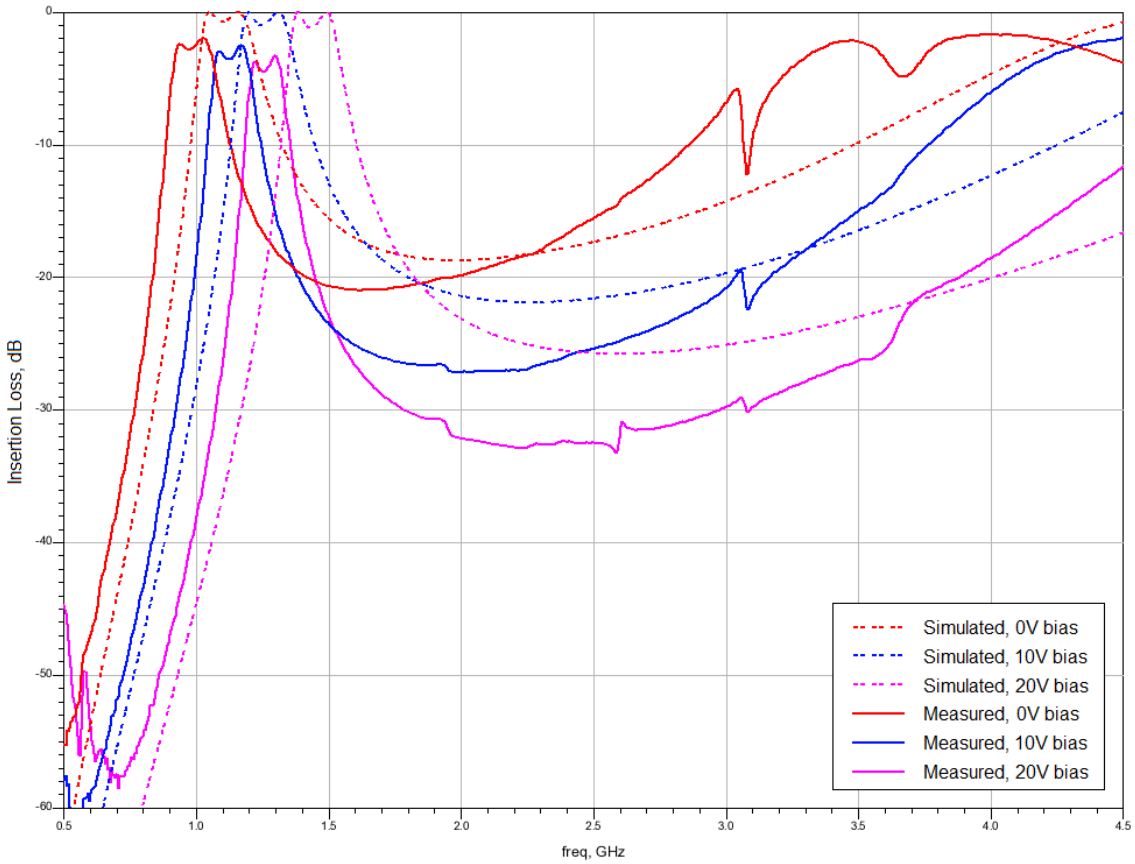

A-1: Simulation with ideal lumped elements vs. measured results of first NRI filter layout with 10nH shunt inductors, and 0.8pF and 0.3pF series capacitors.

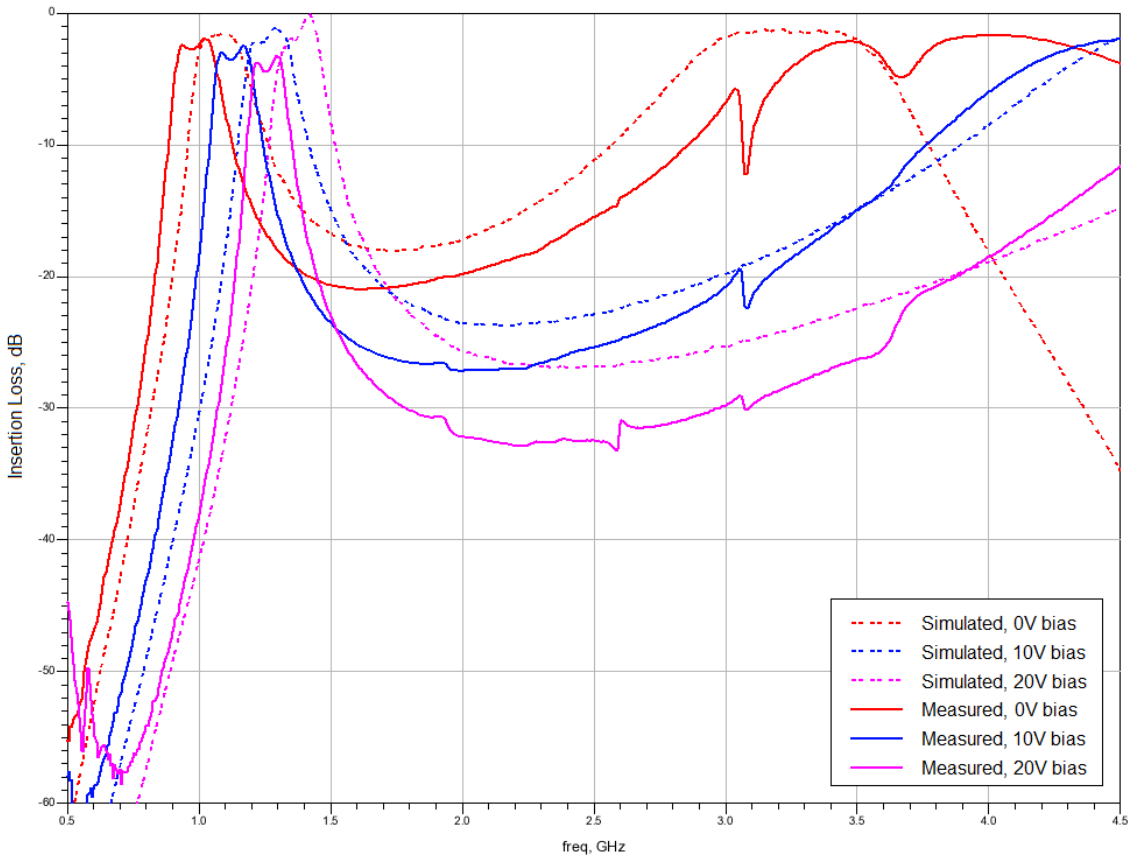

A-2: Simulation with vendor supplied models vs. measured results of first NRI filter layout with 10nH shunt inductors, and 0.8pF and 0.3pF series capacitors.

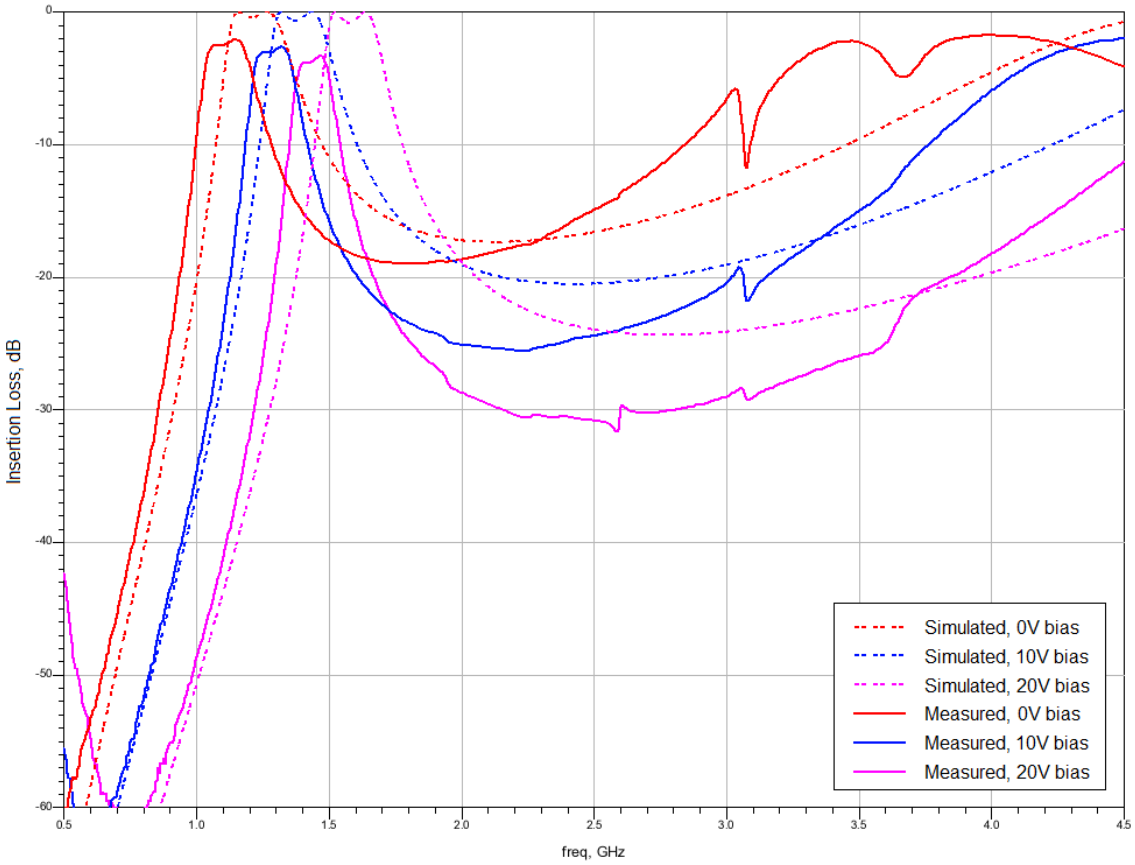

A-3: Simulation with ideal lumped elements vs. measured results of first NRI filter layout with 8.2nH shunt inductors, and 0.8pF and 0.3pF series capacitors.

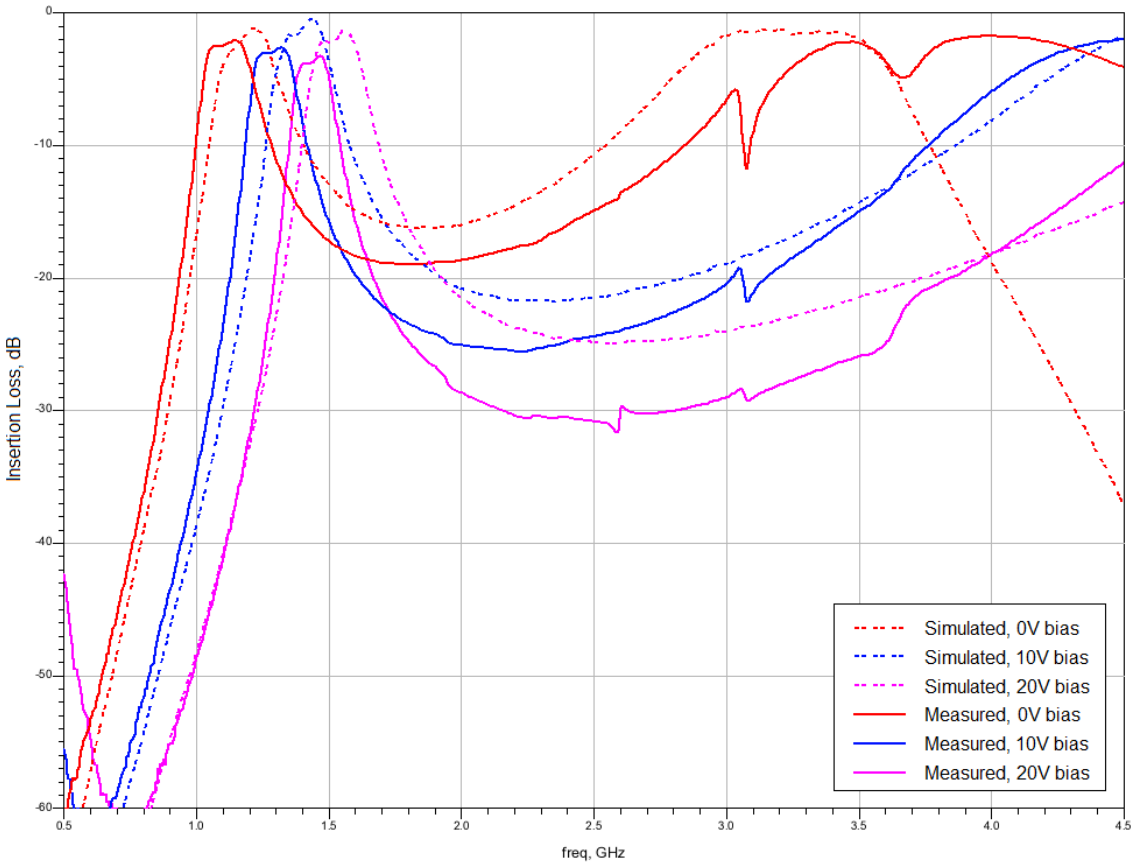

A-4: Simulation with vendor supplied models vs. measured results of first NRI filter layout with 8.2nH shunt inductors, and 0.8pF and 0.3pF series capacitors.

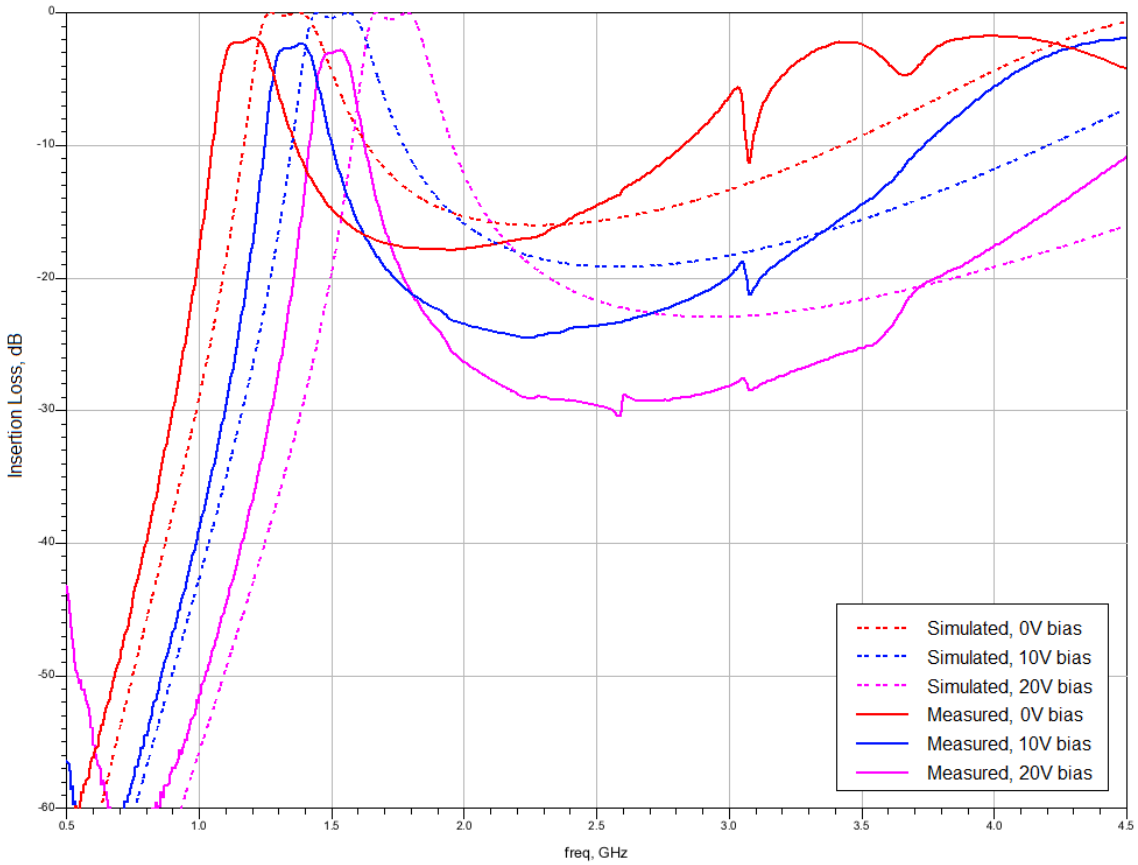

A-5: Simulation with ideal lumped elements vs. measured results of first NRI filter layout with 6.8nH shunt inductors, and 0.8pF and 0.3pF series capacitors.

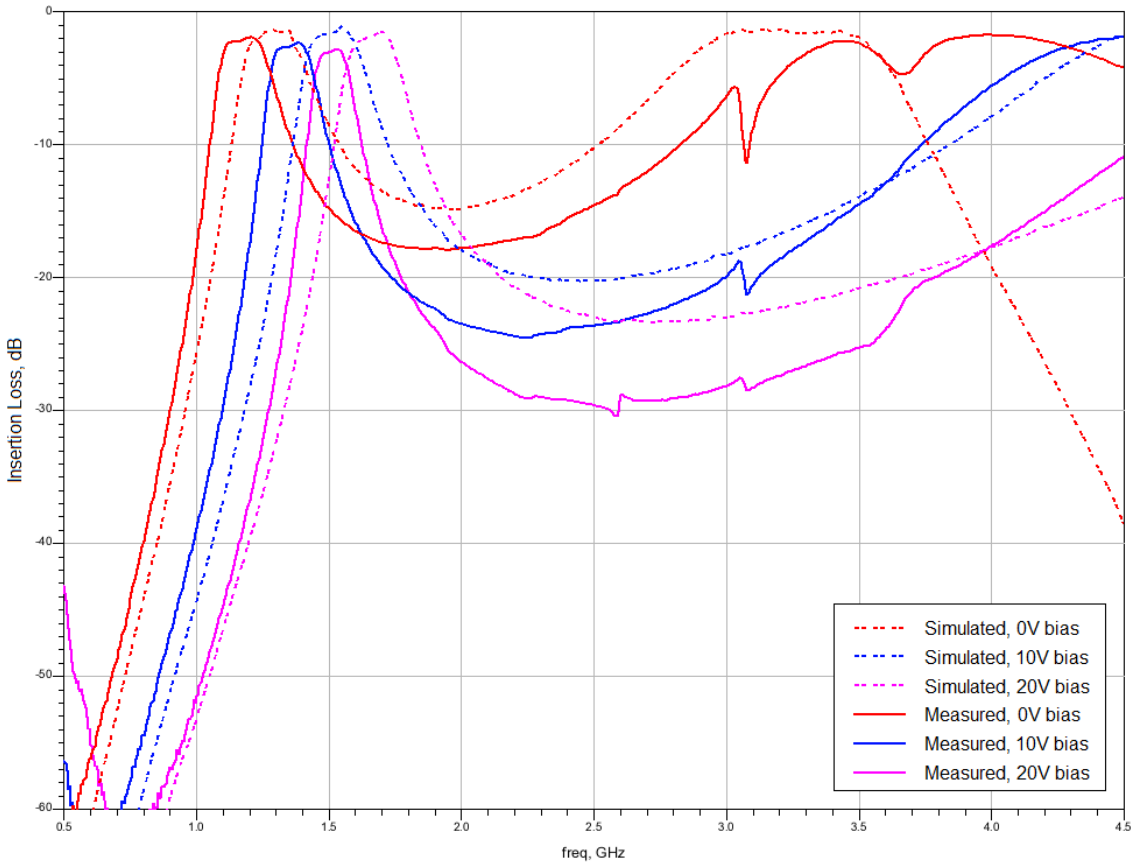

A-6: Simulation with vendor supplied models vs. measured results of first NRI filter layout with 6.8nH shunt inductors, and 0.8pF and 0.3pF series capacitors.

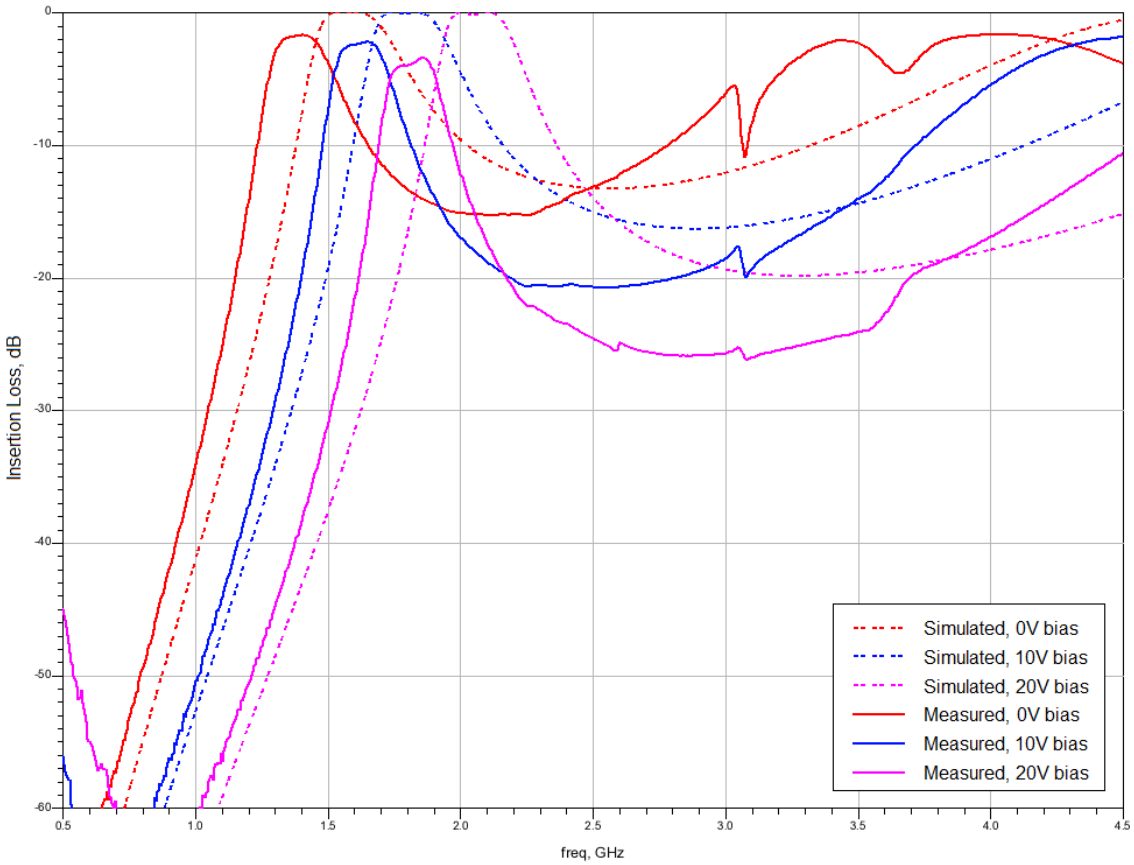

A-7: Simulation with ideal lumped elements vs. measured results of first NRI filter layout with 4.7nH shunt inductors, and 0.8pF and 0.3pF series capacitors.

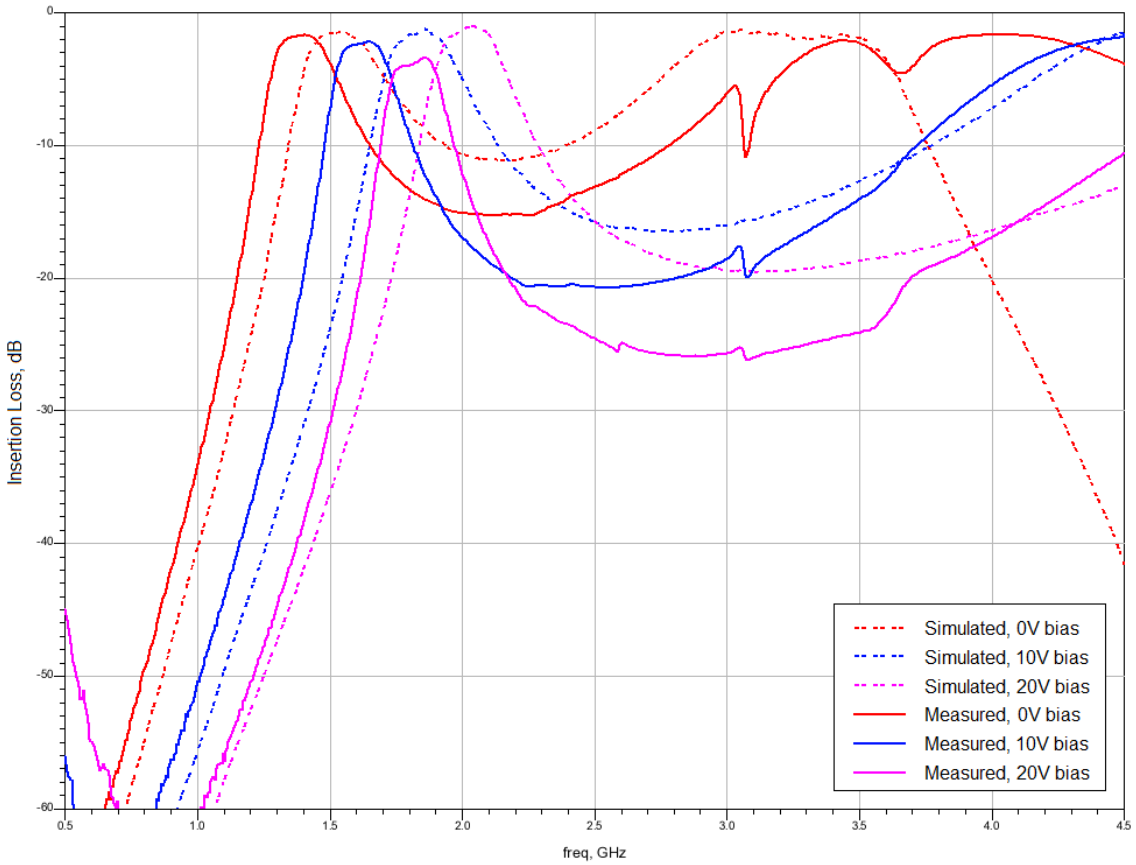

A-8: Simulation with vendor supplied models vs. measured results of first NRI filter layout with 4.7nH shunt inductors, and 0.8pF and 0.3pF series capacitors.

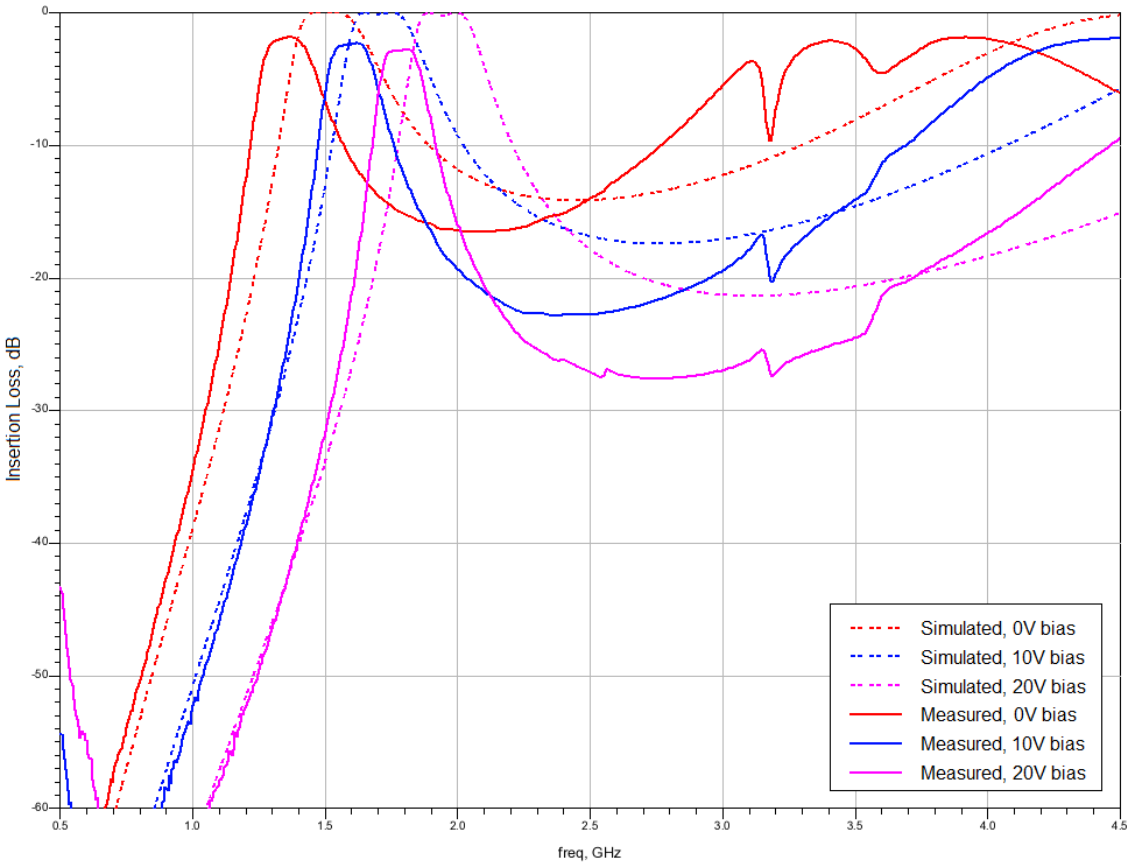

A-9: Simulation with ideal lumped elements vs. measured results of second NRI filter layout with 4.7nH shunt inductors, and 0.8pF and 0.3pF series capacitors.

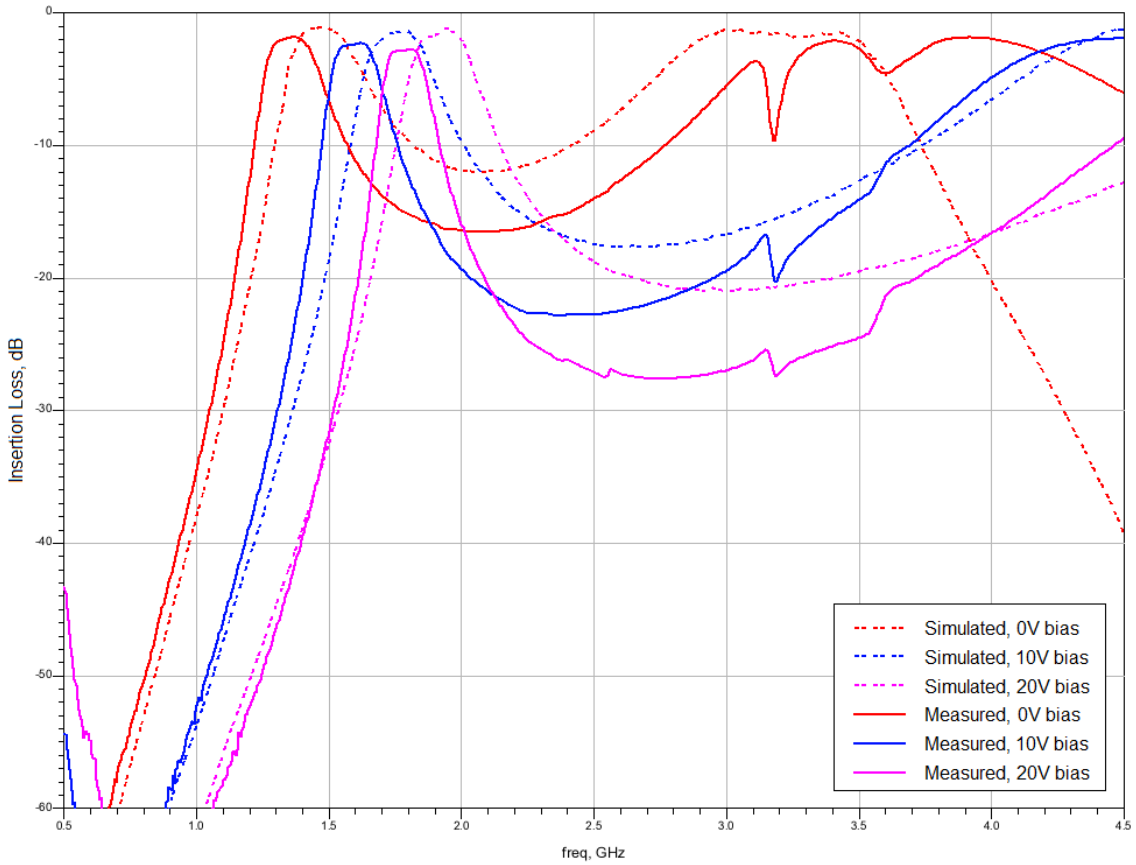

A-10: Simulation with vendor supplied models vs. measured results of second NRI filter layout with 4.7nH shunt inductors, and 0.8pF and 0.3pF series capacitors.

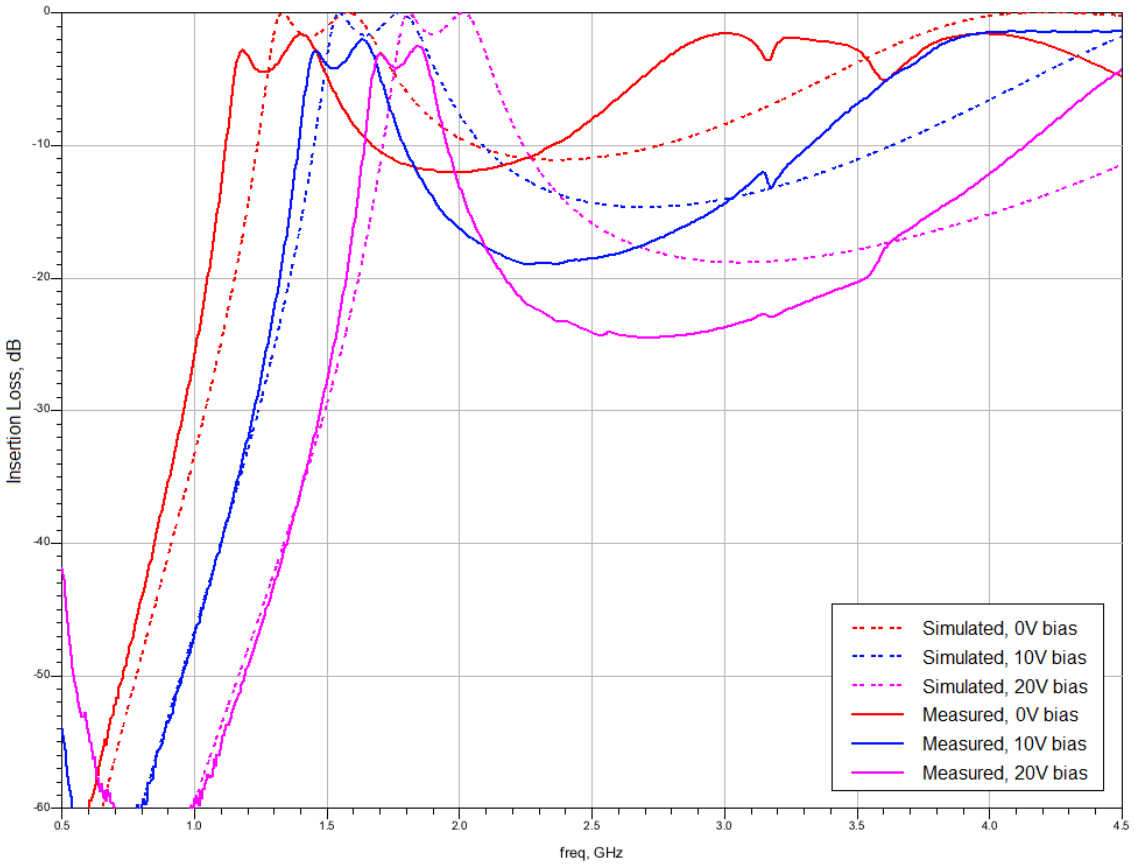

A-11: Simulation with ideal lumped elements vs. measured results of second NRI filter layout with 4.7nH shunt inductors, and 0.8pF and 0.5pF series capacitors.

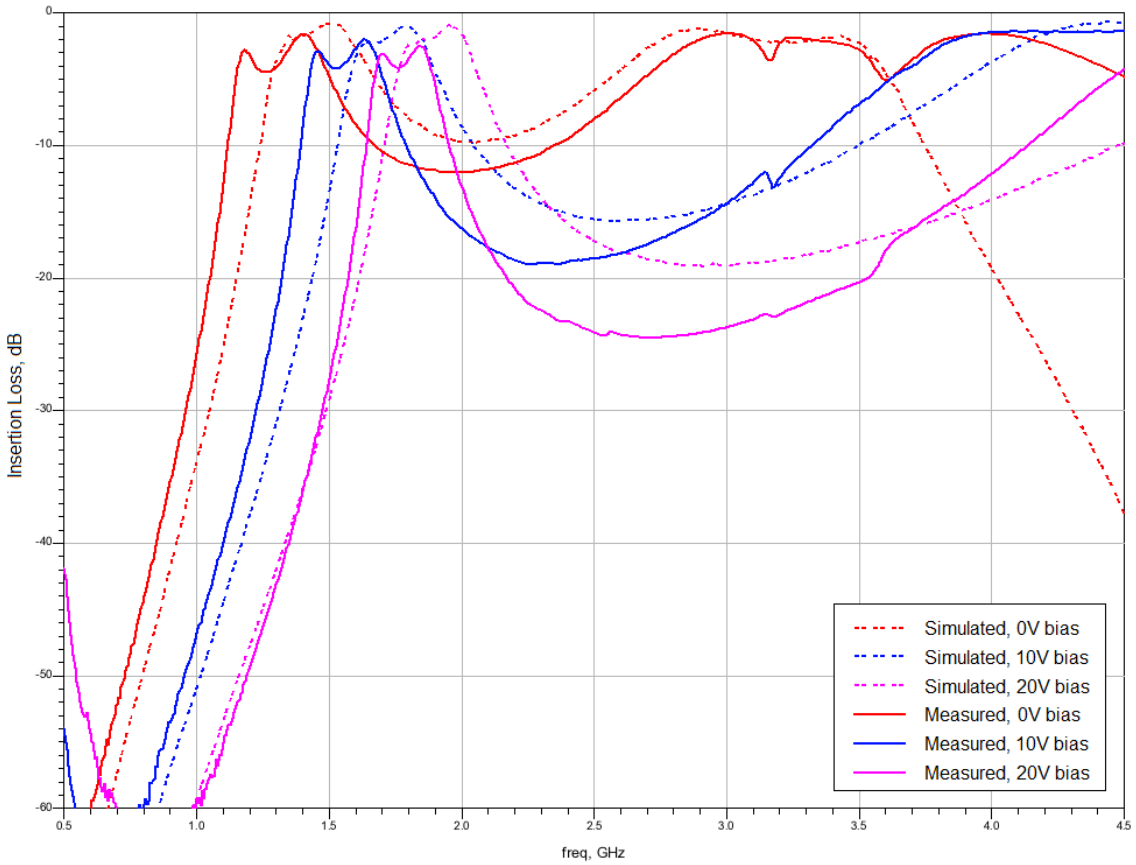

A-12: Simulation with vendor supplied models vs. measured results of second NRI filter layout with 4.7nH shunt inductors, and 0.8pF and 0.5pF series capacitors.

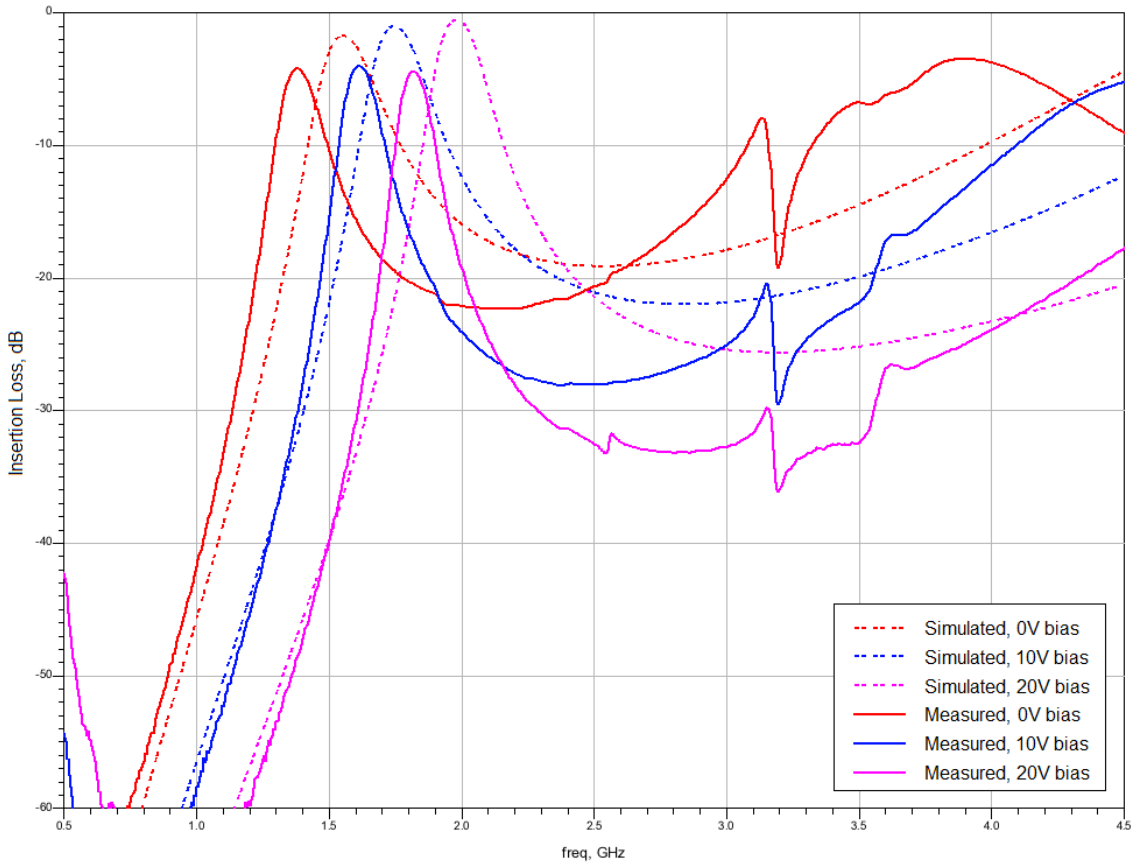

A-13: Simulation with ideal lumped elements vs. measured results of second NRI filter layout with 4.7nH shunt inductors, and 0.8pF and 0.15pF series capacitors.

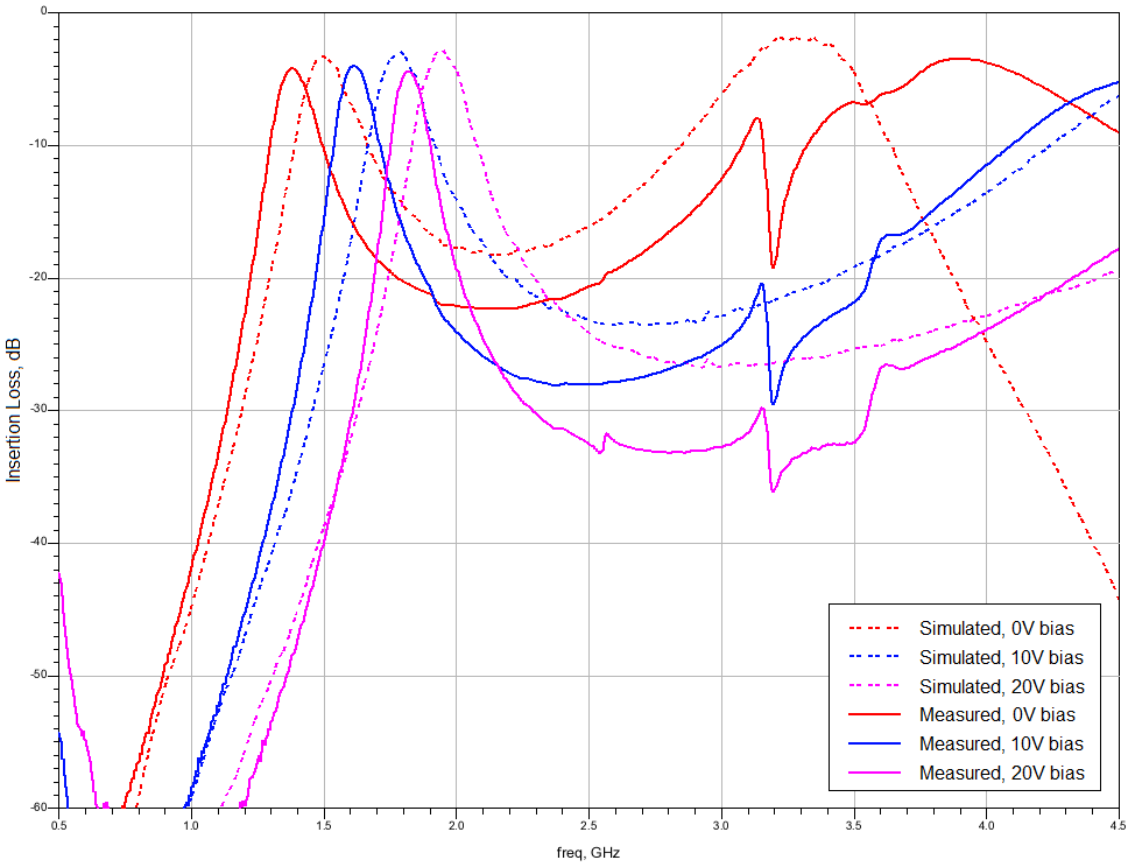

A-14: Simulation with vendor supplied models vs. measured results of second NRI filter layout with 4.7nH shunt inductors, and 0.8pF and 0.15pF series capacitors.

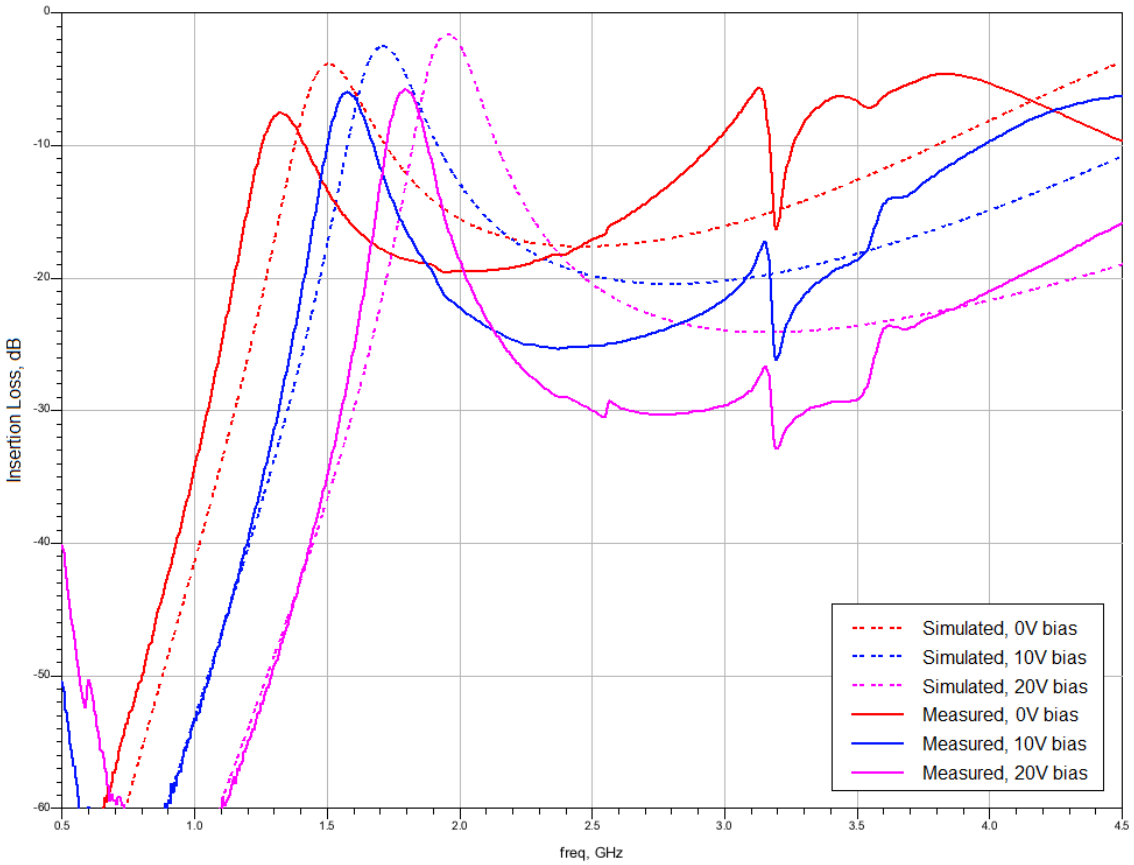

A-15: Simulation with ideal lumped elements vs. measured results of second NRI filter layout with 4.7nH shunt inductors, and 1.0pF and 0.15pF series capacitors.

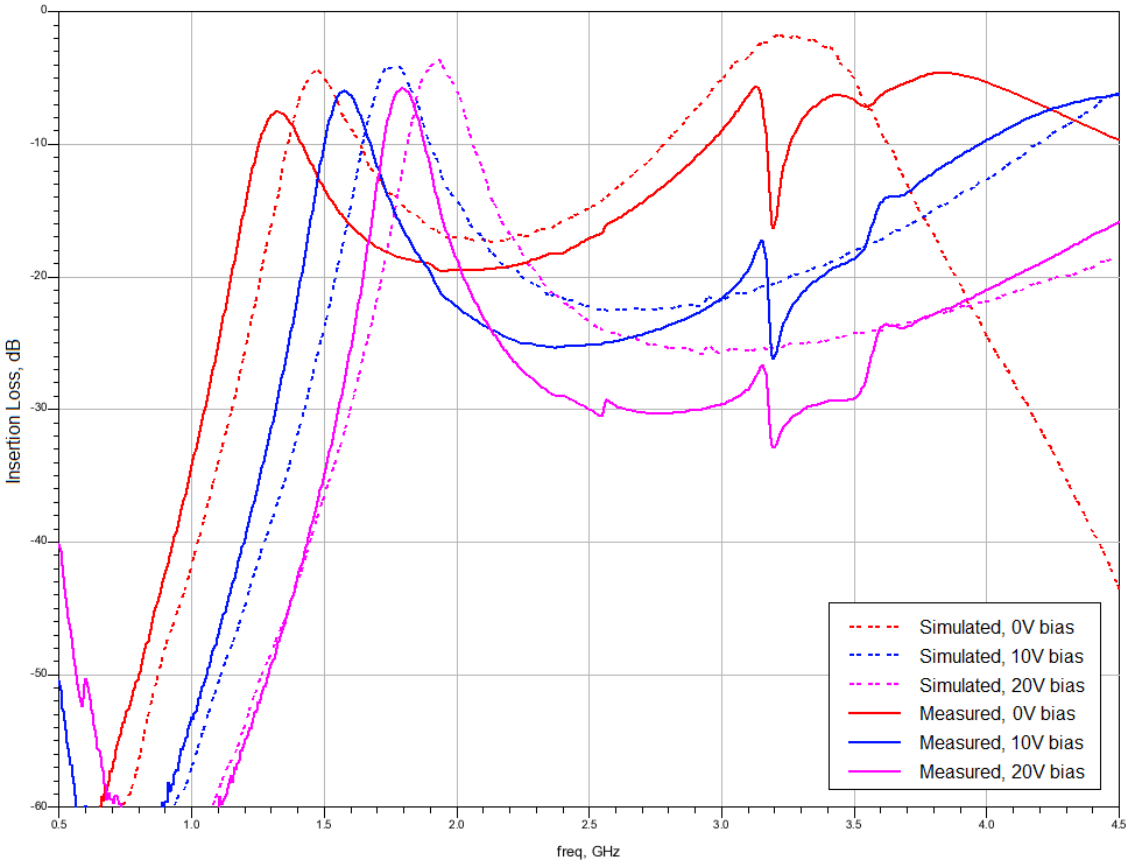

A-16: Simulation with vendor supplied models vs. measured results of second NRI filter layout with 4.7nH shunt inductors, and 1.0pF and 0.15pF series capacitors.

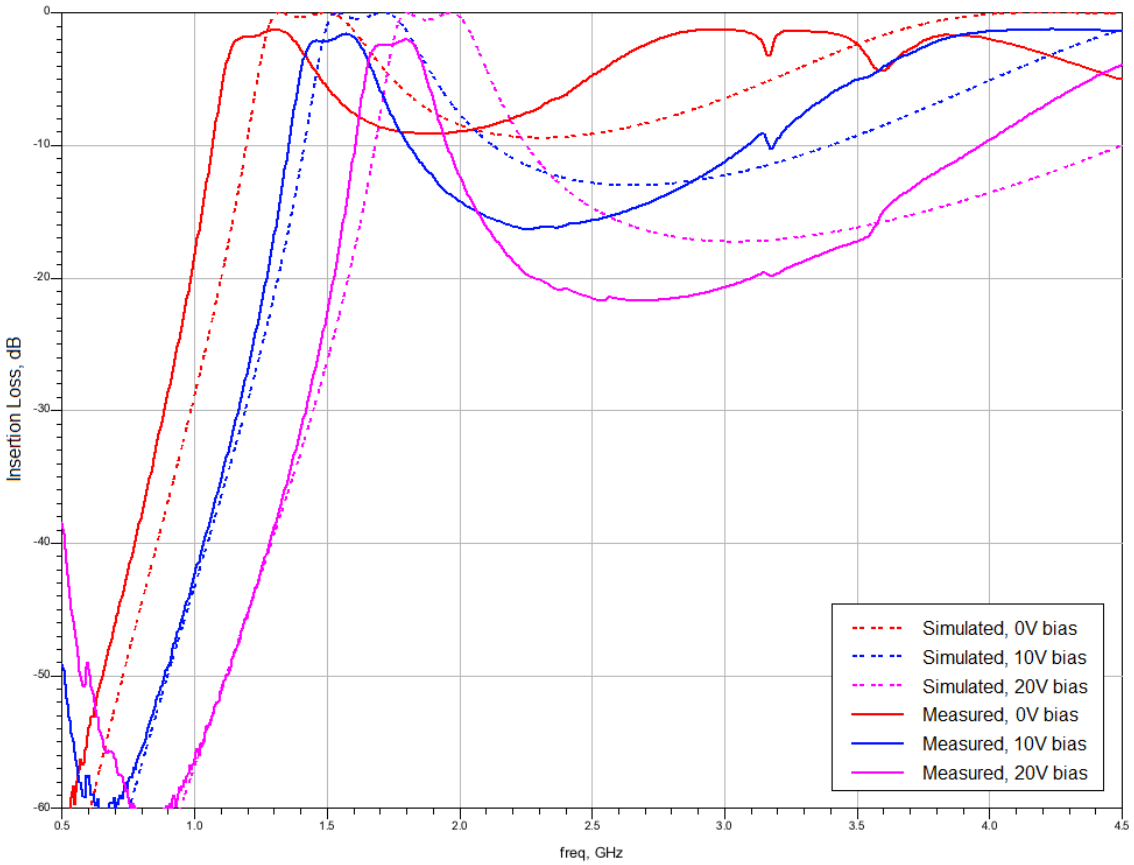

A-17: Simulation with ideal lumped elements vs. measured results of second NRI filter layout with 4.7nH shunt inductors, and 1.0pF and 0.5pF series capacitors.

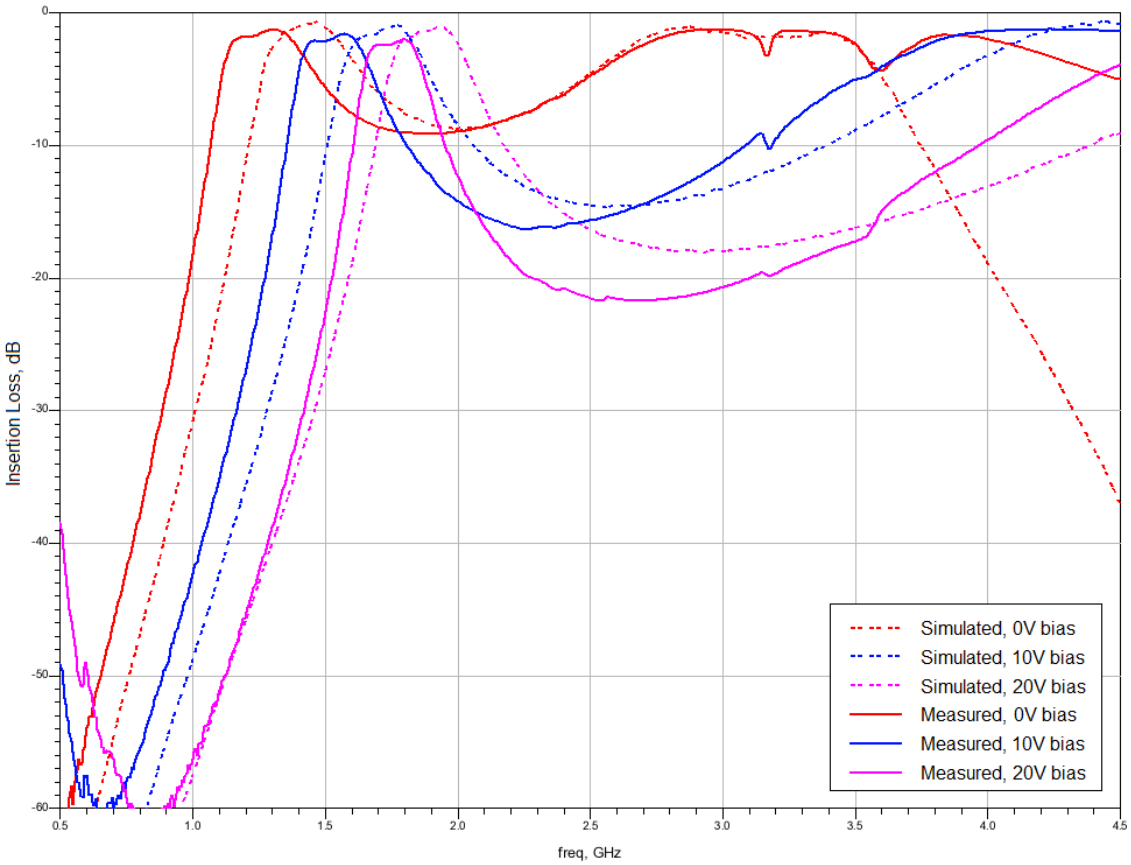

A-18: Simulation with vendor supplied models vs. measured results of second NRI filter layout with 4.7nH shunt inductors, and 1.0pF and 0.5pF series capacitors.

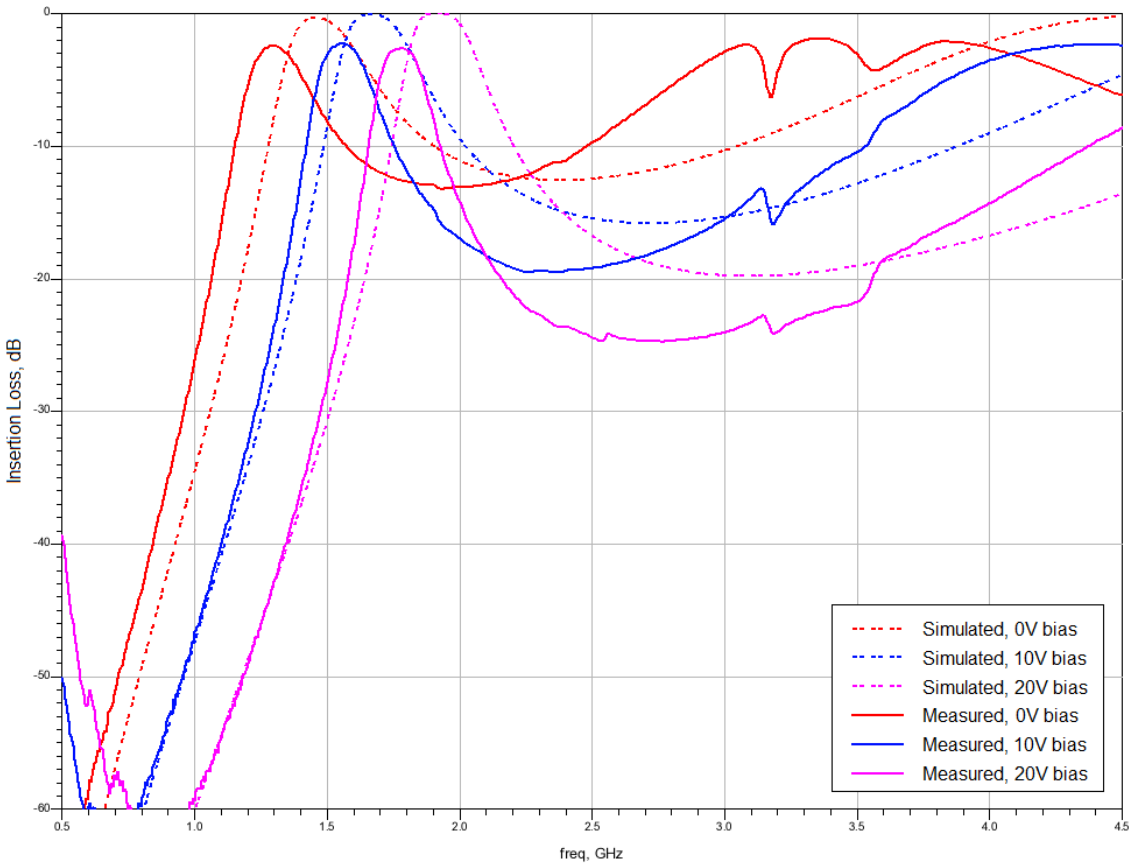

A-19: Simulation with ideal lumped elements vs. measured results of second NRI filter layout with 4.7nH shunt inductors, and 1.0pF and 0.3pF series capacitors.

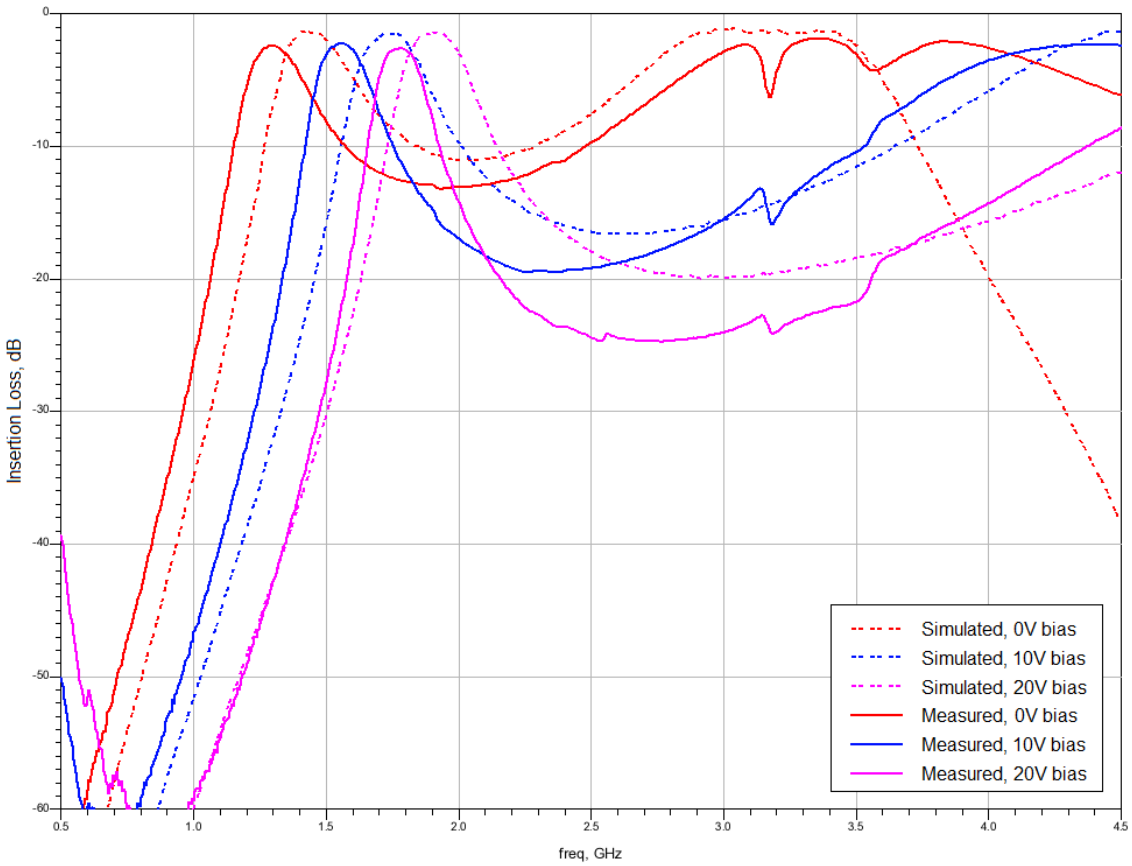

A-20: Simulation with vendor supplied models vs. measured results of second NRI filter layout with 4.7nH shunt inductors, and 1.0pF and 0.3pF series capacitors.

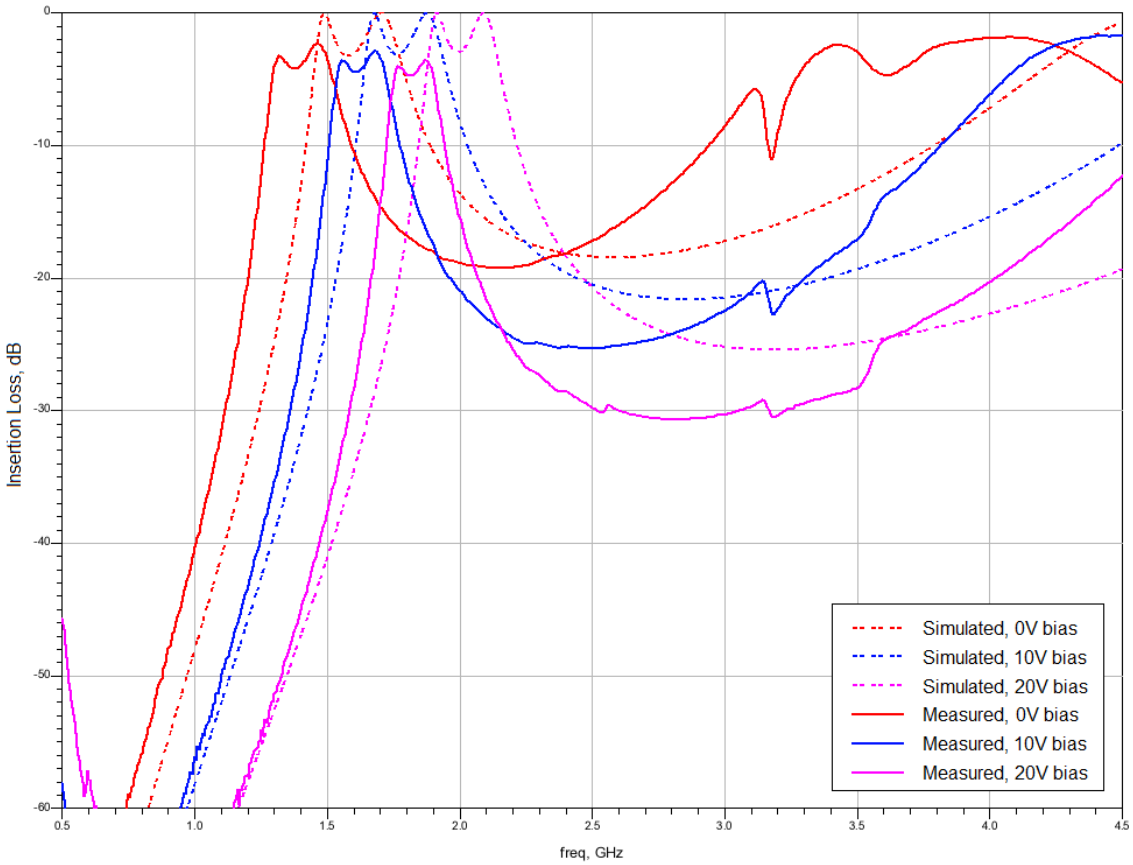

A-21: Simulation with ideal lumped elements vs. measured results of second NRI filter layout with 4.7nH shunt inductors, and 0.5pF and 0.3pF series capacitors.

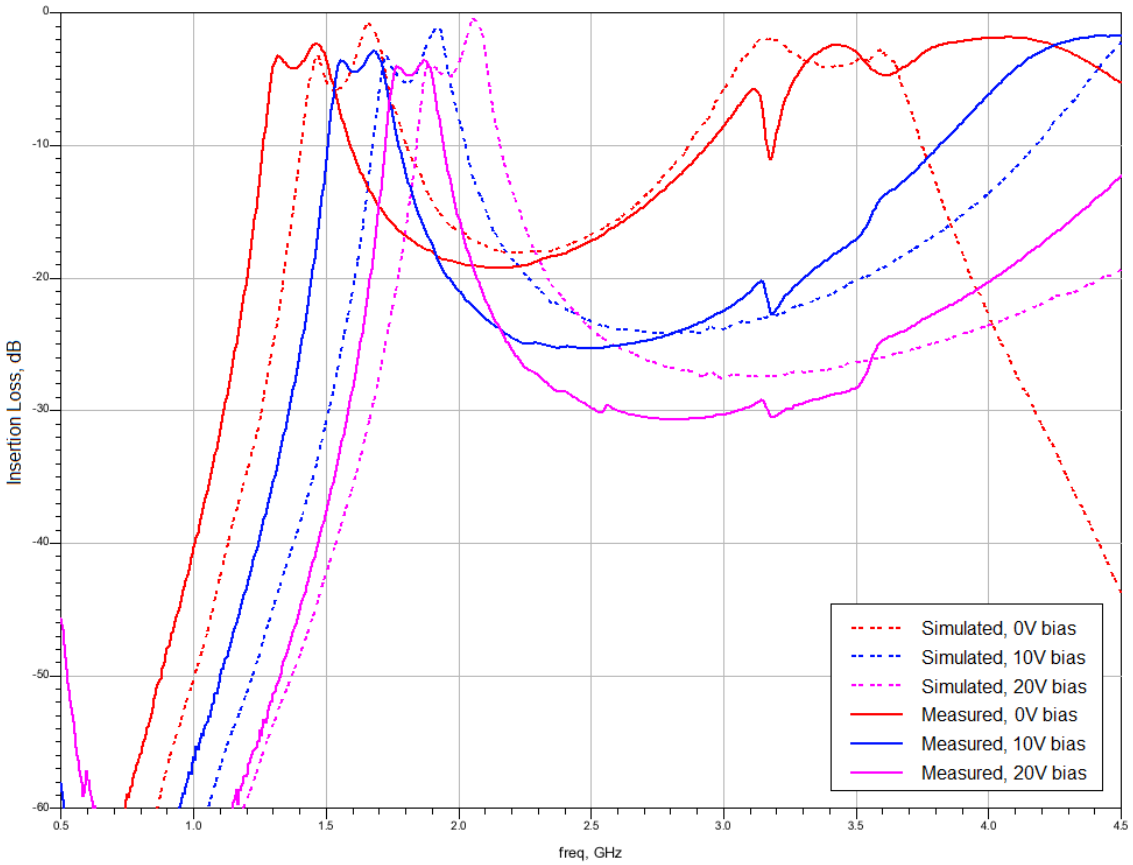

A-22: Simulation with vendor supplied models vs. measured results of second NRI filter layout with 4.7nH shunt inductors, and 0.5pF and 0.3pF series capacitors.

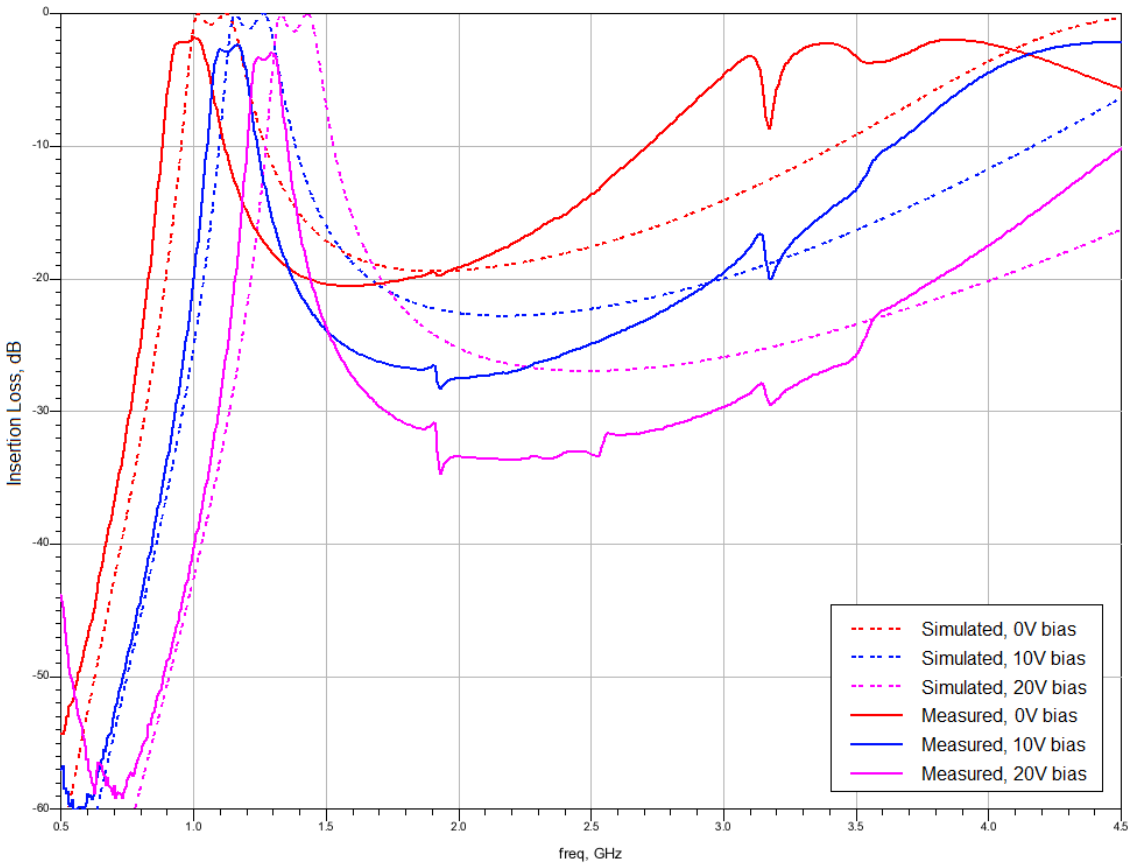

A-23: Simulation with ideal lumped elements vs. measured results of second NRI filter layout with 10nH shunt inductors, and 0.8pF and 0.3pF series capacitors.

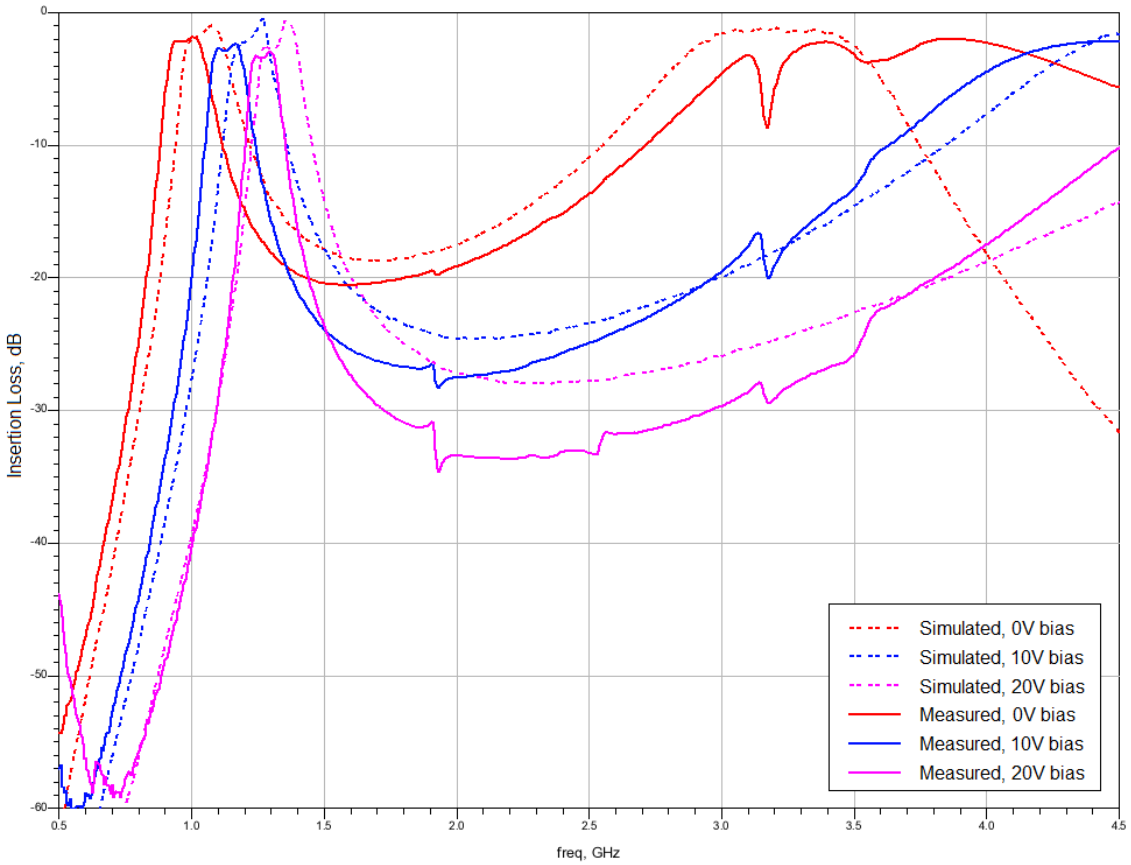

A-24: Simulation with vendor supplied models vs. measured results of second NRI filter layout with 10nH shunt inductors, and 0.8pF and 0.3pF series capacitors.

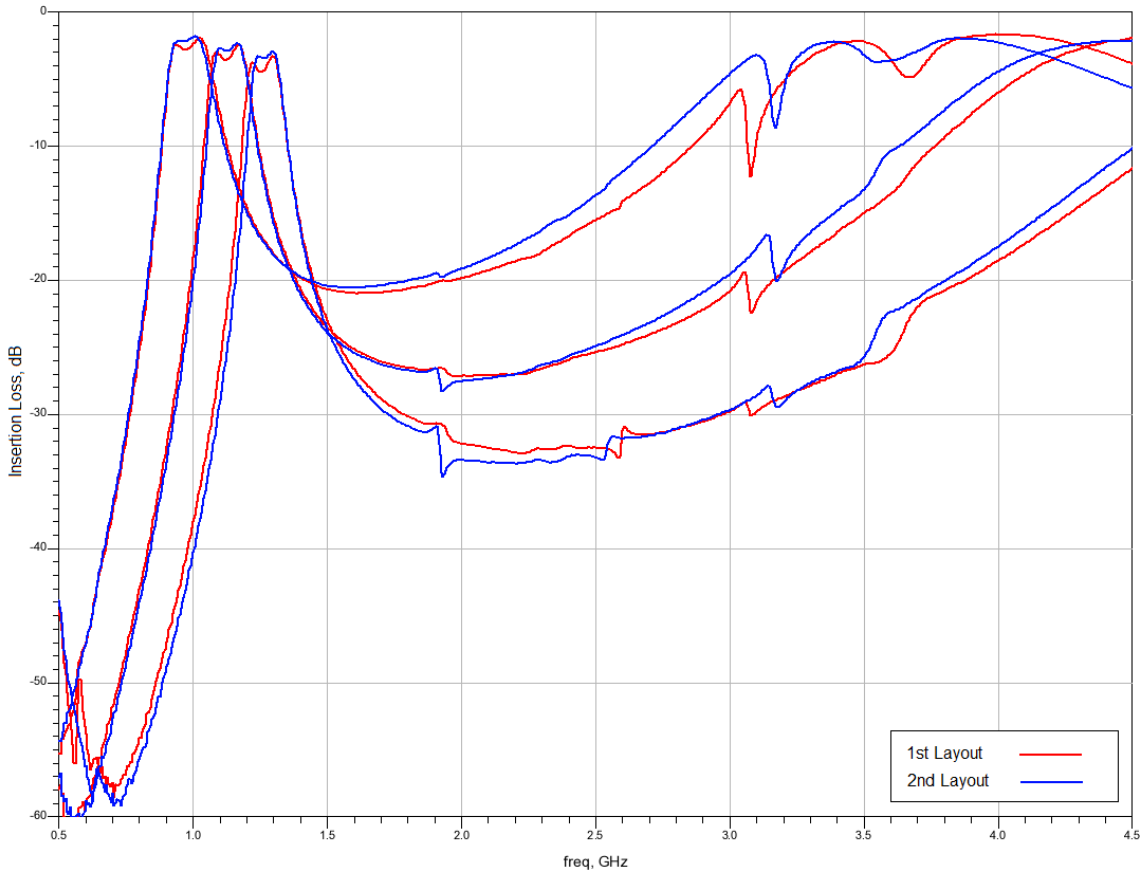

A-25: Comparison of measured results from first and second NRI filter layouts with 10nH shunt inductors, and 0.8pF and 0.3pF series capacitors.

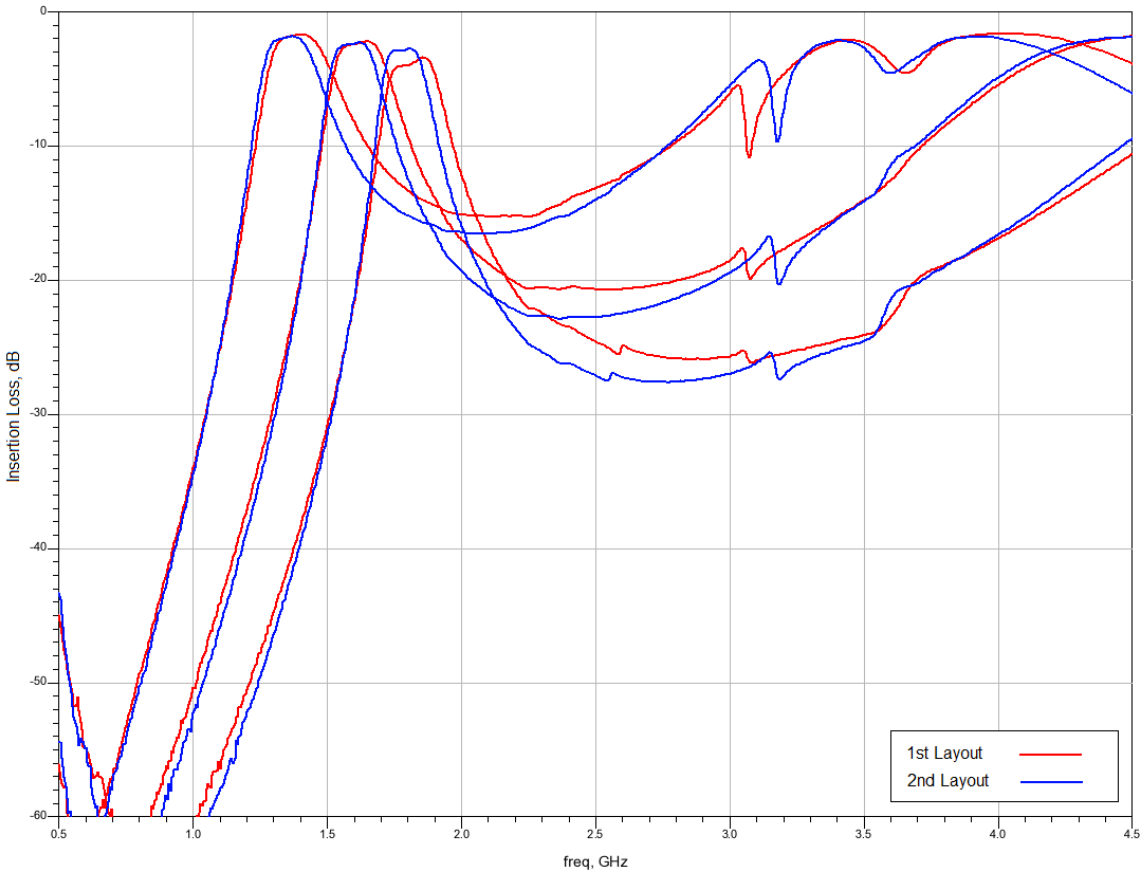

A-26: Comparison of measured results from first and second NRI filter layouts with 4.7nH shunt inductors, and 0.8pF and 0.3pF series capacitors.

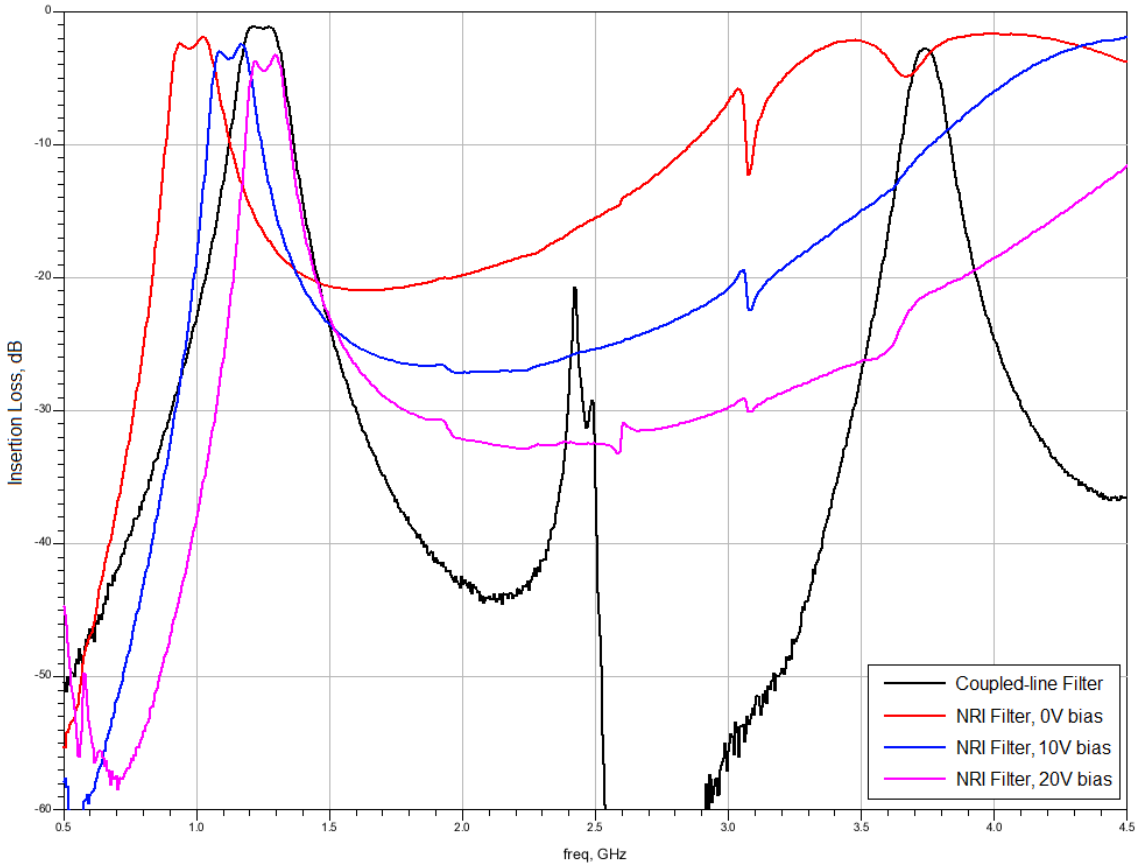

A-27: Comparison of measured results from parallel coupled-line filter and first NRI filter layout with 10nH shunt inductors, and 0.8pF and 0.3pF series capacitors.

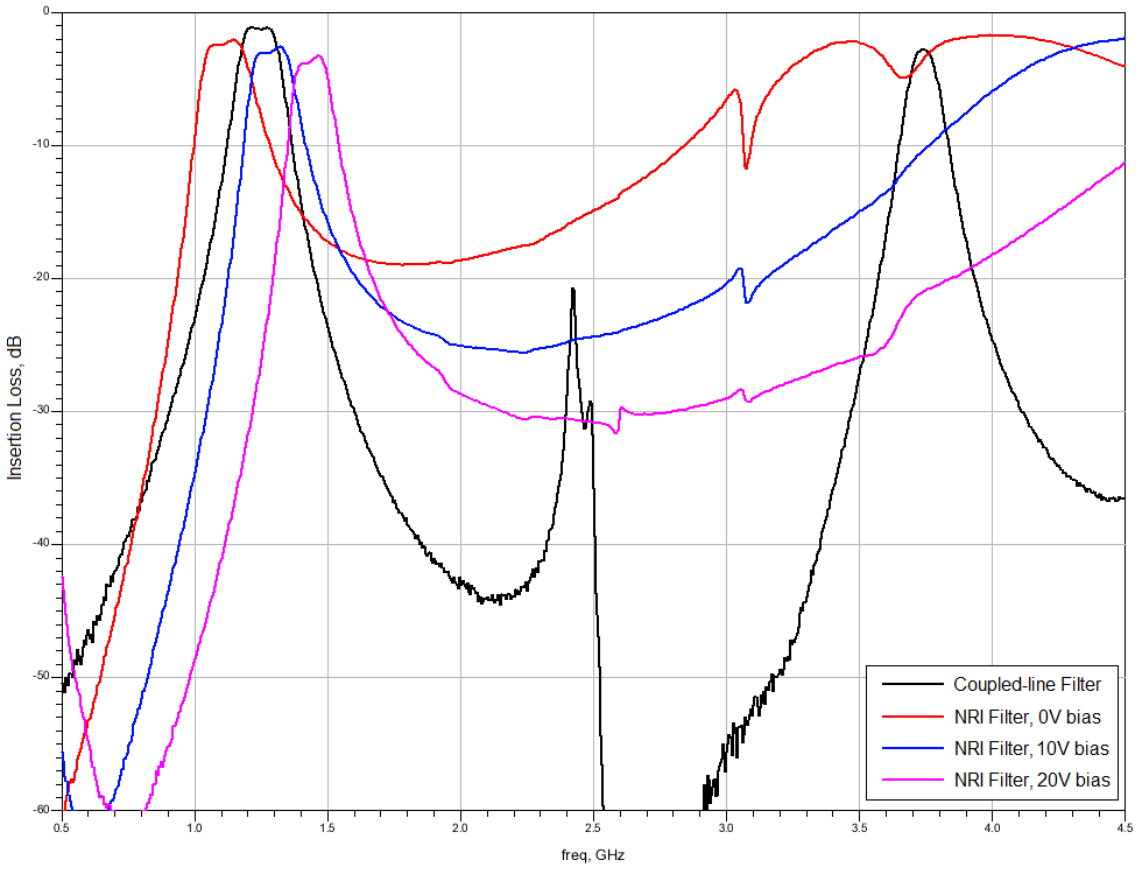

A-28: Comparison of measured results from parallel coupled-line filter and first NRI filter layout with 8.2nH shunt inductors, and 0.8pF and 0.3pF series capacitors.

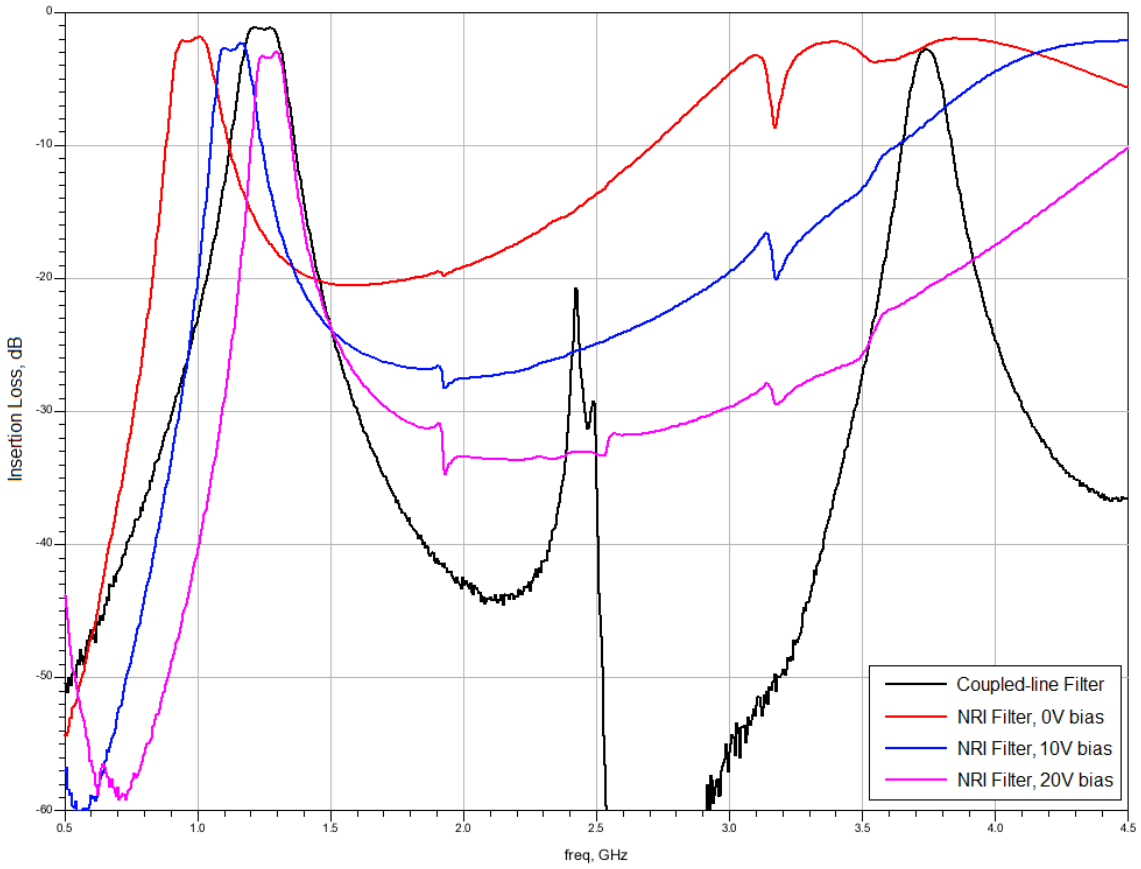

A-29: Comparison of measured results from parallel coupled-line filter and second NRI filter layout with 10nH shunt inductors, and 0.8pF and 0.3pF series capacitors.

VITA

Brian Patrick Lewis received his Master of Science in electrical engineering at Texas A&M University in 2011, as well as his Bachelor of Science in electrical engineering in 2003. He is currently employed by ESCG and is supporting the development of the Orion S-band communication system at NASA's Johnson Space Center. His professional interests include antenna and phased array design and testing, transponder design, and component modeling.

Mr. Lewis may be reached at P.O. Box 777, Brownsboro, TX 75756. His email address is brian.patrick.lewis@gmail.com.